bioRxiv preprint doi: https://doi.org/10.1101/2022.08.11.503617; this version posted October 17, 2022. The copyright holder for this preprint (which was not certified by peer review) is the author/funder, who has granted bioRxiv a license to display the preprint in perpetuity. It is made available under aCC-BY 4.0 International license.

Cryo-ET of infected cells reveals that a succession of two lattices drives vaccinia virus assembly

Miguel Hernandez-Gonzalez[1], Thomas Calcraft[2], Andrea Nans[3], Peter B Rosenthal[2] and Michael Way[1, 4] *

[1]Cellular signalling and cytoskeletal function laboratory, The Francis Crick Institute, 1 Midland Road, London, NW1 1AT, UK

[2]Structural Biology of Cells and Viruses Laboratory, The Francis Crick Institute.

[3]Structural Biology Science Technology Platform, The Francis Crick Institute.

[4] Department of Infectious Disease, Imperial College, London W2 1PG, UK

*To whom correspondence should be addressed. Email: michael.way@crick.ac.uk

Running title: Cryo-ET of vaccinia infected cells

bioRxiv preprint doi: https://doi.org/10.1101/2022.08.11.503617; this version posted October 17, 2022. The copyright holder for this preprint (which was not certified by peer review) is the author/funder, who has granted bioRxiv a license to display the preprint in perpetuity. It is made available under aCC-BY 4.0 International license.

Abstract

During its cytoplasmic replication, vaccinia virus assembles non-infectious spherical immature virions (IV) coated by a viral D13 lattice. Subsequently, IV mature into infectious brick-shaped intracellular mature virus (IMV) that lack D13. Here, we performed cryo-electron tomography of frozen-hydrated vaccinia-infected cells to structurally characterise the maturation process in situ. During IMV formation a new viral core forms inside IV with a wall consisting of trimeric pillars arranged in a new pseudohexagonal lattice. This lattice appears as a palisade in cross-section. During maturation, which involves a 50% reduction in virion volume, the viral membrane becomes corrugated as it adapts to the newly formed viral core in a process that does not appear to require membrane removal. Our study suggests that the length of this core is determined by the D13 lattice and that the consecutive D13 and palisade lattices control virion shape and dimensions during vaccinia assembly and maturation.

bioRxiv preprint doi: https://doi.org/10.1101/2022.08.11.503617; this version posted October 17, 2022. The copyright holder for this preprint (which was not certified by peer review) is the author/funder, who has granted bioRxiv a license to display the preprint in perpetuity. It is made available under aCC-BY 4.0 International license.

Introduction

Poxviruses are large double stranded DNA viruses that replicate and assemble their virions in cytoplasmic perinuclear viral factories [1]. The family includes variola virus, the causative agent of smallpox, and monkeypox as well as vaccinia, the most studied family member which was used as the vaccine to eradicate smallpox [2,3]. During its replication cycle, vaccinia initially assembles into infectious intracellular mature virions (IMV), which are released when infected cells lyse [4]. Prior to cell lysis, however, some IMV become enveloped by a Golgi cisterna or endosomal compartment to form intracellular enveloped virions (IEV) [5-7] (Figure 1A). IEV undergo kinesin-1 mediated microtubule transport to the plasma membrane, where they fuse to release extracellular enveloped virions (EEV), which promotes the long-range spread of infection [8,9]. A proportion of these virions, named cell-associated enveloped virus (CEV), induce the formation of an actin tail beneath the virion, which increases the cell-to-cell spread of the virus [10-13].

The first step in the spread of vaccinia infection is the assembly of IMV, which are the precusor to all subsequent forms (IEV, EEV and CEV) of the virus. IMV formation is initiated when endoplasmic reticulum (ER) associated viral membrane assembly proteins (VMAPs) promote the formation of isolated membrane crescents in the cytoplasm of infected cells [14-16]. The characteristic dimensions and shape of the crescents are determined and maintained by the D13 scaffolding viral protein, which forms trimers that assemble into a hexameric lattice coating the outer surface of these membranes [14,15,17,18]. In vitro structural analysis of recombinant D13 reveals it has a double-jelly-roll structure composed of 8 antiparallel ß-strands that self assembles into a honeycomb lattice of pseudo-hexagonal trimers [19-22]. Ultimately, membrane crescents develop into spherical immature virions (IV) which encapsidate the viral genome and proteins required to produce an IMV [15,17,18,23]. In a process that is still not understood but involves the proteolytic cleavage of viral proteins and the formation of disulphide bonds, spherical IV undergo a dramatic reorganization into brick-shaped IMV [24,25]. During this maturation process, the D13 honeycomb lattice is lost, and a biconcave viral core, containing the viral genome, assembles inside the IV [23]. The outer layer of the viral core forms a paracrystalline palisade-like structure that has been reported to be discontinuous [23,26,27]. In addition, two dense proteinaceous aggregates, known as the lateral bodies, form in the cavity between the outer viral membrane and the biconcave viral core [23,26,28].

Vaccinia virion assembly has been extensively studied. Nevertheless, the key structural determinants that govern the changes occurring during the IV to IMV transistion, as well as

bioRxiv preprint doi: https://doi.org/10.1101/2022.08.11.503617; this version posted October 17, 2022. The copyright holder for this preprint (which was not certified by peer review) is the author/funder, who has granted bioRxiv a license to display the preprint in perpetuity. It is made available under aCC-BY 4.0 International license.

those that define the IMV, remain unknown. To obtain detailed ultra-structural insights into this maturation process, we have now performed cryo-electron tomography (cryo-ET) of vaccinia infected cells, imaging IV as well as infectious IMV in the cytoplasm. Using subtomogram averaging we determine the structure of the D13 lattice on the IV membrane. Moreover, subtomogram averaging of the IMV core reveals a continuous pseudohexagonal palisade lattice, which is reminiscent of a viral capsid. Our analysis also identifies novel features of the surrounding IMV membrane. We discuss a model for maturation from IV to IMV which is organised by the succession of the distinct D13 and palisade lattices.

Results

Electron cryo-tomography of vaccinia virus in infected cells

Cryo-tomograms of thin cellular regions containing IV and IMV were recorded from the periphery of HeLa cells infected with vaccinia virus for 8 hours (Figure 1B, C and S1, Movie 1 and 2). IV, fully coated by the viral D13 lattice, are largely spherical and have a diameter of 351.89 ± 2.88 nm (Table S1). Analysis of tomograms in 3D, however, reveals that a proportion of IV despite being closed and fully coated by D13 have a single invagination of the viral membrane (Figure 1B). This suggests that the D13 lattice is flexible and can accommodate both positive and negative curvatures present on virions with invaginations. This D13 lattice flexibility is also evident from its ability to coat the exterior of "open spheres" with different membrane curvature (also known as crescents due to their shape when seen in a middle view) during IV formation (Figure 2A, B and Movie 3).

The interior of the majority of IV, which contain viral DNA and proteins required for virion assembly, are homogenous and lack any of the distinctive regions or layers seen in IMV (Figure 1B). In a few cases, however, we could observe a single dense striated structure inside IV corresponding to the nucleoid (viral DNA genome and associated proteins) (Figure 2C and S2), as seen in previous ultra-structural analysis of thin EM sections of vaccinia infected cells [28]. We also found examples of related striated structures in the cytoplasm adjacent to, or in direct association with, assembling IV (Figure 2D, E). Consistent with the interpretation that the example shown in Figure 2E represents the viral genome being inserted into assembling IV, structured illumination microscopy together with deconvolution (125 nm resolution) also reveals the presence of elongated DNA structures associating with virions, identified by RFP-A3, in the viral factory (Figure 2F). Our 3D tomographic observations of assembling IV using cryo-ET were consistent with previous ultra-structural analysis of vaccinia infected cells using electron microscopy [16-18,29,30].

bioRxiv preprint doi: https://doi.org/10.1101/2022.08.11.503617; this version posted October 17, 2022. The copyright holder for this preprint (which was not certified by peer review) is the author/funder, who has granted bioRxiv a license to display the preprint in perpetuity. It is made available under aCC-BY 4.0 International license.

In situ structure of the hexagonal D13 lattice

Structural analysis of recombinant D13 in isolation has provided a detailed molecular understanding of the D13 trimer [19-22]. However, the macromolecular arrangements of the D13 lattice on IV in infected cells have largely been studied by deep-etch EM [17,18]. Given the clear lattices present on the IV surface in our tomograms (Figure 3A, Movie 4), we analysed the structure of the D13 lattice in situ by subtomogram averaging. We obtained maps by averaging surface sectors revealing hexamers of trimer arrangements with a lattice spacing of 133 Å, in agreement with lattices described for in vitro assembled D13 and deep-etch EM honeycombs (Figure 3B). Rigid-body docking of the high-resolution structure of a D13 trimer (PDB: 7VFE) into the map shows the packing of D13 trimers is consistent with that recently reported [19]. While at much lower resolution, precluding a detailed description of interface residues, the arrangement of D13 on the spherical IV surface does not appear to include a relative twist of trimeric axes between adjacent trimers as observed in single particle dimers or tubular assembles.

From the hexagonal packing of D13 in the subtomogram average, we estimate that ~5,300 D13 trimers will cover the surface of a spherical IV. The packing density and radius of the D13 lattice on IV are compatible with an icosahedrally symmetric architecture with a triangulation number (T) in the neighborhood of 268. We have not confirmed the presence of icosahedral symmetry, which would require pentameric arrangements of D13 trimers, such as those that have been identified in vitro [19]. Finally, we observed a gap of ~5.6 nm between the innermost surface of the D13 lattice and the membrane of the IV. This gap cannot be explained by any unresolved N- or C-terminal residues of D13 and must therefore be bridged by another protein such as A17 [21].

Structure of intracellular mature virus in infected cells

The internal organisation, dimensions and shape of IMV, which are brick-shaped membrane-bound virions, contrast dramatically with those of IV (Figure 1). Analysis of the size and shape of IMV in 3D reveals they can be approximated to a triaxial ellipsoid of 352 x 281 x 198 nm with a calculated volume of 1.02 x 10^7 nm^3 (Figure 4, Table S1 & Movie 5). The viral membrane of IMV lacks D13 and is heavily corrugated, in contrast to the IV membrane, which is smooth (Figure 4, Figure S3). In addition, there is a new additional outer layer of 6.67 ± 0.11 nm on the viral membrane that was not present on IV (Figures 4 and 5A-B). Underneath the viral membrane there is a palisade-looking structure consisting of a series of turret-like densities in cross-section (12.5 nm thick), which is associated with a inner wall that is 3.84 ± 0.09 nm thick (Figure 5A). Depending on the orientation of the virion, the interior

bioRxiv preprint doi: https://doi.org/10.1101/2022.08.11.503617; this version posted October 17, 2022. The copyright holder for this preprint (which was not certified by peer review) is the author/funder, who has granted bioRxiv a license to display the preprint in perpetuity. It is made available under aCC-BY 4.0 International license.

organisation of the IMV appears very different. In the mid view of its two widest dimensions (352 x 281 nm), the palisade appears in contact with the viral membrane. However, in the orthogonal lateral view (352 x 198 nm) the palisade structure, which only contacts the viral membrane at the ends of the virion, presents two concavities (Figure 5B). Each cavity contains a single dense and amorphous structure, termed lateral body. The distance between the viral membrane and the palisade varies between 9.28 ± 0.18 nm and 46.53 ± 2.72 nm, the latter being where the lateral bodies are accommodated (see Table S1 for detailed measurements). 3D tomographic analyses reveal that the palisade is a semi-regular array as in the view from above (Figure 5C, D).

The semi-regular organisation of the palisade is most apparent in naked cores, which lack the viral membrane and are occasionally found in the cytoplasm (Figure 6A, B). Segmentation of our 3D tomograms reveals the palisade is a continuous structure without fenestrations that defines the boundary of the virus core, including the regions that contact the lateral bodies (Figure 5E, Movie 6). Inside the core, there are no obvious higher order structures. There are, however, interconnected densities that vary between virions but tend to accumulate beneath the inner wall of the core (Figure 5A). These densities are especially apparent in the compressed region underneath the lateral bodies (Figure 5C). Such densities associated with the inner wall of the core potentially represent the viral genome and its associated proteins given its high contrast. Another characteristic that is evident in midplane views of approximately half of the IMV (48.9%, n = 94), is that one corner of the virion (and in a few cases, two corners) appears as a straight or flattened "cut corner" (Figure 1C and Figure S3). This characteristic is intrinsic to the core wall as it is also apparent in naked cores (Figure 6A, Movie 7) and is also evident in previous published electron micrographs of cores obtained from purified IMV particles [27]. In addition, these naked cores lack the two densities corresponding to lateral bodies but have associated spaghetti-like structures contacting the palisade surface (Figure 6A). These flexible polymers, which are 2.6 nm in diameter, form an exclusion zone of ~ 40 nm around the naked core (Figure 6A). Furthermore, it was noticeable that naked cores have randomly distributed ring like structures on their surface that were not observed in IMV. These rings seem to protrude 10-20 nm from the palisade surface and had inner and outer diameters of 4.5 ± 0.1 nm and 9.9 ± 0.1 nm, respectively (Figure 6C).

The corrugated membrane and hexagonal core lattice of vaccinia virions

During viral egress, some IMV become triple-membraned intracellular enveloped virions (IEV) after envelopment by a Golgi cisterna or endosomal compartment (Figure 1A).

bioRxiv preprint doi: https://doi.org/10.1101/2022.08.11.503617; this version posted October 17, 2022. The copyright holder for this preprint (which was not certified by peer review) is the author/funder, who has granted bioRxiv a license to display the preprint in perpetuity. It is made available under aCC-BY 4.0 International license.

Subsequent fusion of the IEV with the plasma membrane releases double-membraned extracellular enveloped virions (EEV) that are known as cell-associated extracellular enveloped virions (CEV) if they remain attached to the outside of the cell [7]. Our tomograms reveal that the additional membranes acquired by envelopment are smooth and not corrugated as observed for the IMV membrane (Figure 7). In the case of IEV, the outermost membrane is also not always in close contact with the underlying membrane (see Table S1 for virion measurements). The dimensions and structure of the inner IMV and corrugated membrane are also unaffected by envelopment (Figure 7B). Notably, the palisade fully coats the viral core in all infectious virions and its organisation appears unaltered (Figures 7A and 8A). To study the architecture of the palisade, we performed subtomogram averaging separately using IMV, IEV and CEV/EEV particles. Maps obtained from the different virion types, all displayed the same organisation and lattice parameters (P6 symmetry with a=b=89 ± 2 Å, θ=120°) (Fig S4). A new combined map obtained by averaging all particle types together, reveals that the palisade is composed of trimeric pillars with projecting lobes that interact with neighbouring pillars with local hexagonal symmetry (Figure 8B). These pillars are embedded in an unfeatured inner wall. While further details are required to understand its molecular composition, this arrangement appears to be flexible enough to assemble a continuous biconcave capsid structure.

Maturation of IV to IMV

Radical changes in the organisation, dimensions and shape of IV result in the formation of IMV (Figure 9). Based on our tomograms, IV have an average diameter of 351.89 ± 2.88 nm and a volume of 2.28 x 10^7 nm^3 for completely spherical particles (Figure 9A). In contrast, "brick-shaped" IMV have a volume of 1.02 x 10^7 nm^3 based on dimensions of 352 x 281 x 198 nm (Figure 9A). This reduction in volume is accompanied by a dramatic corrugation of the viral membrane, together with the loss of the D13 lattice (Figure 4). To better characterise membrane corrugation, we measured the middle-plane perimeter of the viral membrane in IV and IMV, following the wrinkles of the viral membrane to obtain its contour length. We found that the membrane contour is virtually identical in IV and IMV, as well as in the equivalent innermost membrane of EEV/CEV (~1100 nm, Figure 9B). This suggests the viral membrane folds during maturation, which would explain the reduction in volume without any detectable loss of membrane surface. In addition to reducing their volume by ~50%, IVs also change their shape when they mature into IMV, becoming a triaxial ellipsoid. Strikingly, the longest IMV dimension matches the diameter of IV (Figure 9A, B), suggesting that the major axis of IMV is determined by the IV diameter. In our tomograms we also found particles that may represent intermediates and/or defective examples of IV maturation. These

bioRxiv preprint doi: https://doi.org/10.1101/2022.08.11.503617; this version posted October 17, 2022. The copyright holder for this preprint (which was not certified by peer review) is the author/funder, who has granted bioRxiv a license to display the preprint in perpetuity. It is made available under aCC-BY 4.0 International license.

include examples where the palisade is fully formed but the viral membrane, which either lacks or is partially coated with D13, is not associated with the viral core (Figure 9C). It is also interesting that we did not observe any virions with partially formed cores suggesting that palisade formation is likely to be rapid or occur en bloc.

Discussion

Previous ultra-structural analyses of vaccinia infected cells by electron microscopy over many decades have provided important insights into the assembly of vaccinia virions. These studies, however, have largely been conducted on fixed sections of infected cells which can have fixation, processing and staining artifacts. Cryo-EM studies, analysing viral entry or purified virions, have demonstrated the potential of using cryo-EM to study vaccinia structure [26,27,31,32]. Here, we apply cryo-ET to image the thin edge of plunge-frozen, vaccinia virus-infected cells, revealing virus architecture in situ. While there is confirmation of past work, important new features emerged from our study. We found that during maturation to IMV, spherical IV lose their D13-coat and reduce their volume by ~50%. During this process, the outer viral membrane becomes corrugated and contacts the capsid-like palisade layer and the lateral bodies. The palisade, which remains unaltered during subsequent virion morphogenesis, is a continuous regular lattice with pseudohexagonal symmetry that defines the viral core boundaries. Our observations suggest that these two lattices, D13 and the palisade, drive vaccinia assembly and maturation.

We found that the D13 lattices coating IV have a similar architecture to the D13 lattices formed in vitro [19]. Furthermore, Hyun et al. produced D13 spherical IV-like particles with a similar diameter to the D13-coated IV we imaged in situ. This strongly suggests that the D13 lattice, which initially curves open membranes and eventually forms closed particles, determines both the size and shape of the IV. In addition, our images and STA maps show that a 5.6-nm gap separates the D13 lattice from the IV membrane. This gap is most likely occupied by A17, which tethers the D13 lattice to the membrane [21,33,34] but whose flexibility would preclude its detection on the IV membrane by cryo-ET. The lack of direct contact of the D13 protein lattice with the viral membrane is reminiscent of clathrin and other vesicle-forming coats in eukaryotic cells where the structural lattice does not directly interact with the membrane to be deformed [35,36]. Instead, an adaptor module mediates the lattice-membrane association. A mechanism by which coat complexes promote membrane curvature is by clustering the adaptor module on the membrane to be deformed [37,38]. Therefore, D13-mediated clustering of A17 could promote membrane deformation during IV

bioRxiv preprint doi: https://doi.org/10.1101/2022.08.11.503617; this version posted October 17, 2022. The copyright holder for this preprint (which was not certified by peer review) is the author/funder, who has granted bioRxiv a license to display the preprint in perpetuity. It is made available under aCC-BY 4.0 International license.

formation. In addition, A17 can also contribute to membrane bending independently of D13, since it can deform membranes in vitro and when expressed in non-infected cells [39].

Despite their relatively constant diameter, a proportion of D13-coated IV have an elongated membrane invagination (Figure 1A). This feature has largely gone unnoticed in previous EM studies imaging thin sections, although IV membrane deformations are apparent in some studies [28,40-43]. While the cause of this membrane buckling remains to be established, it may relate to the thinness of the cell periphery or a consequence of forces on the membrane during IV assembly or DNA insertion into assembling IV [42]. As in other studies, we observe the nucleoid in the IV interior or associated with either open or closed spheres, as previously suggested for DNA entry events [28,30]. It is tempting to speculate that the IV invagination may mark the site of DNA entry and IV sealing of the pore.

The palisade, which is largely composed of p4A and A4 [31,44,45], consists of a trimeric assembly in a pseudo-hexagonal lattice arrangement. Based on the uniformity of the IMV and the relative measurements we obtained of IV and IMV, we conclude that this new viral lattice, which fully covers the core and defines its boundary, dictates the dimensions and shape of IMV. The viral membrane, no longer covered by D13, would wrinkle and adopt the shape and dimensions of the newly formed palisade. This process may also be responsible for the compression of the lateral bodies onto the virus core, causing the biconcave deformation of the latter. The maturation model that emerges from our work provides a simple way by which a membrane-bound particle adapts to a new internal lattice and changes its shape and dimensions to become more compact without membrane removal (Figure 9D). Moreover, our data suggest the palisade length is dictated by the diameter of the IV, which in turn is established by D13. The palisade would grow inside the D13-coated IV until reaching its maximum length, that is the IV diameter. In other words, the D13 lattice limits the longest dimension of the palisade lattice. The size restriction of a growing viral core by its surrounding viral membrane has also been proposed for the assembly of the HIV core [46,47]. Our observation of a viral particle partly coated by D13 with an assembled palisade suggests the palisade forms before D13 disassembles, and also implies that complete removal of D13 is not required for palisade formation (Figure 9C). Moreover, our observations suggest that palisade assembly and D13 removal are coordinated and rapid.

In the IMV, the lateral bodies define a lateral domain, as opposed to the virion tips, which are specified by the long axis of the viral core. The lateral bodies prevent direct interactions between the palisade and the wrinkled viral membrane, which might contribute to the

bioRxiv preprint doi: https://doi.org/10.1101/2022.08.11.503617; this version posted October 17, 2022. The copyright holder for this preprint (which was not certified by peer review) is the author/funder, who has granted bioRxiv a license to display the preprint in perpetuity. It is made available under aCC-BY 4.0 International license.

304 differences between the lateral and the tip domains. Notably, the virion tips are the site of
305 polarisation of the set of viral membrane proteins that form the entry fusion complex (EFC),
306 which is essential for virus infectivity [48-50]. How and when EFC polarity is established is
307 unknown. An appealing possibility is that virion tips are stochastically defined by the growth
308 of the palisade long axis during assembly and the EFC and other viral factors polarise at the
309 virion tips after palisade formation by their exclusion from the lateral domains. In such a
310 scenario, palisade formation would drive virion polarity.

311 The EFC mediates fusion of the IMV membrane with the plasma membrane or an endocytic
312 compartment during entry, which releases a naked core into the cytoplasm [51-55].
313 Subsequently, early proteins are produced by early RNA transcripts released from naked
314 cores, which are essential to liberate the DNA genome into the cytosol to initiate replication
315 [1]. Our cryo-ET data of naked cores in infected cells indicate the palisade structure does not
316 require surrounding membranes for stability. Furthermore, the loss of lateral bodies from
317 naked cores suggests their association with the palisade depends on the IMV membrane. In
318 addition, we observed flexible 2.6-nm thick polymers fully surrounding naked cores that
319 might correspond to either RNA or the viral genome which is released from the naked core.
320 Finally, we detected ring structures protruding from the palisade surface of naked cores.
321 Analysis of these rings reveals they are compatible in dimension with the hexameric rings of
322 the viral D5 primase/helicase, which is essential for vaccinia genome release [56,57]. A similar
323 pore-like structure has been previously described on the surface of vaccinia cores generated
324 by treating purified IMV with NP40 and DTT [58]. In addition, pores in the palisade itself, and
325 not protruding rings, have also been reported in intact purified IMV [26]. Further work is
326 needed to determine the identity and relationship between these pore-like structures, as
327 D5 only associates with naked cores after entry and not newly assembled IMV [56].
328
329 A common feature of many viral families is the use of a three-dimensional lattice, or capsid,
330 which determines the structure and dimensions of the virion. What distinguishes vaccinia
331 from other viruses is that an initial lattice, D13, is replaced by a second lattice, the palisade,
332 during virion assembly. This contrasts African Swine Fever virus (ASFV), which retains its
333 D13-like lattice, in addition to an inner capsid in mature virions [59]. Based on the structural
334 similarities between D13 and the structural components of other viruses with a pseudo-
335 hexameric structure formed by a trimeric protein containing concatenated beta-barrels,
336 vaccinia has been included in the PRD1/adenovirus lineage [60]. However, the viral proteins
337 that form the palisade, which is present in the mature particles, may be just as important
338 as D13 in structural phylogenetic comparisons.

bioRxiv preprint doi: https://doi.org/10.1101/2022.08.11.503617; this version posted October 17, 2022. The copyright holder for this preprint (which was not certified by peer review) is the author/funder, who has granted bioRxiv a license to display the preprint in perpetuity. It is made available under aCC-BY 4.0 International license.

The palisade is a regular capsid-like structure determining the morphology of all four forms of infectious vaccinia virions (IMV, IEV, EEV and CEV). This palisade is surrounded by a heavily corrugated membrane. Our study shows that the palisade and the corrugated viral membrane are invariant defining features of all types of infectious virions. The additional membranes acquired by envelopment are different to the IMV viral membrane as they are not corrugated or always in close contact with the IMV surface (Figure 7). Moreover, the acquisition of these membranes is not associated with major changes in the virion structure or palisade architecture (Figure 7 and 8). This suggests that these additional membranes are used to facilitate viral egress before cell lysis. In fact, these membranes and associated proteins drive IEV transport on microtubules to the cell periphery, IEV fusion with the plasma membrane and subsequent actin-based transport of CEV [7-11,13]. In contrast, the IMV membrane serves to contain the viral core and lateral bodies and organises the essential components required for entry and, also, envelopment during viral morphogenesis. Based on the strong protein conservation between orthopoxviruses, we believe that the virion assembly of monkeypox and variola major are likely to be identical to that of vaccinia virus we have described here.

Methods

Recombinant viruses

To facilitate cryo-ET observations, we produced recombinant Western Reserve vaccinia strains lacking F11 to prevent cells from rounding-up early during infection [61]. In addition, the A36-YdF mutation was used to abolish actin tail formation beneath CEV [11,13,62]. The F11 gene was deleted in A36 YdF [8] or A36 YdF ΔNPF1-3 [63] backgrounds using the same targeting strategy as previously described [64]. Fluorescence was used as a selectable marker to isolate recombinant ΔF11-mCherry viruses by successive rounds of plaque purification in BS-C-1 cells. Correct gene replacement was confirmed by PCR, sequencing of the F11 locus and western blot analysis.

Cell growth, vaccinia infection and vitrification

HeLa cells were maintained in complete MEM (supplemented with 10% Fetal Bovine Serum, 100 ug/ml streptomycin and 100 U/ml penicillin) at 37 °C with 5% CO_2. Cells were washed with PBS, treated with trypsin, seeded on glow discharged (40 sec at 45 mA) Quantifoil R3.5/1 gold grids of 200 mesh and placed in wells of 6-well plates with complete MEM. After overnight growth, the cells were infected with A36-YdF ΔF11 or A36-YdF ΔNPF1-3 ΔF11 vaccinia strains in serum-free MEM at a multiplicity of infection of 2. After one hour, the medium was replaced with complete MEM. At 8 hours post infection grids were washed once

bioRxiv preprint doi: https://doi.org/10.1101/2022.08.11.503617; this version posted October 17, 2022. The copyright holder for this preprint (which was not certified by peer review) is the author/funder, who has granted bioRxiv a license to display the preprint in perpetuity. It is made available under aCC-BY 4.0 International license.

with PBS and excess PBS was removed with a Whatman paper before blotting and vitrification using the Vitrobot Mark IV System, which was set to 95% relative humidity at 22°C. Colloidal gold particles (10-nm diameter) were pipetted onto grids before blotting, which was performed for 14 s with a relative force of -10.

Cryo-electron tomography, image processing and analyses

Grids were first screened on a Talos Arctica TEM (Thermo Fisher) to select edges of cells with an abundance of viral particles that were thin enough for cryo-ET. Selected grid regions were registered before transferring to a Titan Krios (Thermo Fisher), where the mapped grid selections were re-imaged. The Titan Krios was fitted with a K2 Summit direct detector (Gatan) operated in electron counting mode. A Gatan GIF energy filter was used in zero-loss mode with a 20 eV slit width. Dose-symmetric tilt series were collected from -57° to +57° at a 3° increment, a pixel size of 4.31 Å and a defocus of -8 µm using Tomography 5.7 software (Thermo Fisher) (Table S2). Four movie frames were collected per tilt with a dose of 1.7 e/Å^2 per tilt, giving a cumulative dose of 66.3 e/Å^2 per tilt series. Movie frames were aligned using alignframes from IMOD [65]. Tilt series were aligned using gold fiducials or patch tracking in IMOD. Contrast transfer function (CTF) correction and tomogram reconstruction were also implemented in IMOD [65,66]. Alternatively, tomograms were CTF-corrected and reconstructed using novaCTF [67]. In both cases, a SIRT-like filter equivalent to 5 iterations was applied. Segmentations were manually performed (AMIRA, Thermo Fisher), mainly on tomograms that were denoised using ISONet with CTF deconvolution and missing-wedge filling from deep learning [68].

The IV diameter, the axes of IMV and their perimeters, and the major axes of IEV and EEV were measured in 3dmod from IMOD using a middle plane of each viral particle. For perimeters, the viral membranes were manually traced to measure their total contour length. As reported previously [23], virions with the side view perpendicular to the electron beam, in which two concavities of the core are visible, were much less frequent than other views. Because of this, for the calculation of the minor axis of IMV we measured the minor axis of both IMV and IMV inside EEV. This is also the reason why we did not find enough side views of IEV to directly measure their minor axis (Table S1). To estimate the IEV minor axis, we measured the thickness that the additional IEV membranes add, and combined it to the calculated IMV minor axis. For volumes calculation, we assumed IV are perfectly spherical and IMV, IEV and EEV triaxial elipsoids.

bioRxiv preprint doi: https://doi.org/10.1101/2022.08.11.503617; this version posted October 17, 2022. The copyright holder for this preprint (which was not certified by peer review) is the author/funder, who has granted bioRxiv a license to display the preprint in perpetuity. It is made available under aCC-BY 4.0 International license.

411 **Subtomogram averaging**

412 Tomograms containing IV or IMV were selected for subtomogram averaging (STA). D13 and
413 palisade particles in immature and mature virions respectively were picked from the bin4
414 SIRT-filtered tomograms using oversampled surface models in Dynamo [69], then imported to
415 Relion 3.1 [70] for subsequent subtomogram averaging. Unless otherwise specified, local
416 angular searches about the initial orientations generated in Dynamo were used throughout
417 data processing. For particle extraction, only unbinned weighted back projections
418 reconstructions from novaCTF were used. Lattice measurements were carried out in real
419 space using ChimeraX [71]. D13 particles were extracted in 96-pixel boxes at the bin2 pixel
420 size of 4.31Å/pixel. An initial reference was generated using reference-free 3D classification
421 without applied symmetry, with the resulting map clearly showing the honeycomb lattice
422 of D13 trimers. Initial classification and refinement was carried out in both C1 and C6
423 symmetries to verify the symmetry of the D13 hexamer-of-trimers. After initial
424 classifications and removing of overlapping particles with a distance cutoff of 50Å, particles
425 were re-extracted without binning (4.31Å/pixel) in 192 pixel boxes. Final refinement in C6
426 symmetry reached 19Å resolution according to the FSC=0.143 criterion.
427
428 Palisade particles were initially extracted at binning level 2 (8.62Å/pixel) in 96-pixel boxes.
429 Initial references were generated using independent reference-free 3D classifications for
430 each virion type. This clearly showed the palisade lattice in every case, and the particles
431 for each virion type were from then on processed independently, but in an identical manner.
432 For each virion type, alternating rounds of 3D classification and refinement were used to
433 centre the palisade particles at 2-fold binning. After convergence at 2-fold binning, particles
434 were re-extracted without binning (4.31Å/pixel) in 128-pixel boxes. Overlapping particles
435 were removed with a distance cutoff of 40Å before further refinements were carried out
436 without binning. As all refinements converged on maps with identical lattices, particles from
437 all virion types except for the naked cores were then combined for further refinements. All
438 refinements were carried out without application of symmetry up to this point. After the
439 C1 maps converged and the symmetry of the lattice was apparent, further refinement runs
440 were carried out with C3 symmetry applied. The final resolutions of the palisade maps
441 ranged from 20-30Å, according to the FSC=0.143 criterion.
442
443 **Immunofluorescence imaging**

444 HeLa cells on fibronectin-coated coverslips were infected with an RFP-A3 vaccinia strain [72]
445 for 8 hours and fixed with 4% paraformaldehyde in PBS for 10 min, then permeabilised with
446 0.1% Triton X-100 in PBS for 5 min and incubated in blocking buffer (10 mM MES pH 6.1, 150

bioRxiv preprint doi: https://doi.org/10.1101/2022.08.11.503617; this version posted October 17, 2022. The copyright holder for this preprint (which was not certified by peer review) is the author/funder, who has granted bioRxiv a license to display the preprint in perpetuity. It is made available under aCC-BY 4.0 International license.

mM NaCl, 5 mM EGTA, 5 mM $MgCl_2$, and 5 mM glucose) containing 2% (v/v) fetal calf serum and 1% (w/v) BSA for 30 min prior to addition of 4′,6-diamidino-2-phenylindole (DAPI) for 5 minutes, before mounting the coverslips using Mowiol. Coverslips were imaged on an Olympus iX83 Microscope with Olympus 150x/1.45 NA X-Line Apochromatic Objective Lens, dual Photometrics BSI-Express sCMOS cameras and CoolLED pE-300 Light Source (Visitech) and was controlled using Micro-Manager 2.0.0. Image stacks of 10-15 z-slices with 0.1 µm steps were acquired and deconvolved using the express deconvolution setting on Huygens Software (Scientific Volume Imaging).

Acknowledgements

We thank Alessandro Costa, Neil McDonald, Jeremy Carlton and as the Way lab (Francis Crick Institute) for insightful comments on the manuscript as well as LuYan Cao for providing the initial slide of infected cells used in our SIM analysis (Fig. 2F). We also acknowledge Philip Walker and Andy Purkiss of the Structural Biology Science Technology Platform and the Scientific Computing Science Technology Platform for computational support. MHG thanks Pauline McIntosh (Francis Crick Institute) for initial guidance and training. The work in the Way and Rosenthal labs was supported by the Francis Crick Institute, which receives its core funding from Cancer Research UK (FC001209 and FC001143), the UK Medical Research Council (FC001209 and FC001143), and the Wellcome Trust (FC001209 and FC001143). The funders had no role in study design, data collection and analysis, decision to publish, or preparation of the manuscript. For the purpose of Open Access, the authors have applied a CC BY public copyright license to any Author Accepted Manuscript version arising from this submission.

Author contributions

All authors designed the research program and strategy. MHG, TC and AN performed research, MHG and TC analyzed data and MHG, TC, PBR and MW wrote the paper.

Competing interests

The authors have no competing financial interests

bioRxiv preprint doi: https://doi.org/10.1101/2022.08.11.503617; this version posted October 17, 2022. The copyright holder for this preprint (which was not certified by peer review) is the author/funder, who has granted bioRxiv a license to display the preprint in perpetuity. It is made available under aCC-BY 4.0 International license.

478 **References**

479

480 1 Moss, B. in *Fields Virology* (ed Howley PM Knipe DM) 2905-2946 (Lippincott Williams
481 and Wilkins, 2007).

482 2 Jacobs, B. L. *et al*. Vaccinia virus vaccines: past, present and future. *Antiviral Res*
483 **84**, 1-13, doi:10.1016/j.antiviral.2009.06.006 (2009).

484 3 Walsh, S. R. & Dolin, R. Vaccinia viruses: vaccines against smallpox and vectors
485 against infectious diseases and tumors. *Expert Rev Vaccines* **10**, 1221-1240,
486 doi:10.1586/erv.11.79 (2011).

487 4 Roberts, K. L. & Smith, G. L. Vaccinia virus morphogenesis and dissemination. *Trends*
488 *Microbiol* **16**, 472-479, doi:10.1016/j.tim.2008.07.009 (2008).

489 5 Schmelz, M. *et al*. Assembly of vaccinia virus: the second wrapping cisterna is derived
490 from the trans Golgi network. *J Virol* **68**, 130-147 (1994).

491 6 Tooze, J., Hollinshead, M., Reis, B., Radsak, K. & Kern, H. Progeny vaccinia and
492 human cytomegalovirus particles utilize early endosomal cisternae for their envelopes. *Eur*
493 *J Cell Biol* **60**, 163-178 (1993).

494 7 Smith, G. L., Vanderplasschen, A. & Law, M. The formation and function of
495 extracellular enveloped vaccinia virus. *J Gen Virol* **83**, 2915-2931, doi:10.1099/0022-1317-
496 83-12-2915 (2002).

497 8 Rietdorf, J. *et al*. Kinesin-dependent movement on microtubules precedes actin-
498 based motility of vaccinia virus. *Nat Cell Biol* **3**, 992-1000, doi:10.1038/ncb1101-992 (2001).

499 9 Leite, F. & Way, M. The role of signalling and the cytoskeleton during Vaccinia Virus
500 egress. *Virus Res* **209**, 87-99, doi:10.1016/j.virusres.2015.01.024 (2015).

501 10 Cudmore, S., Cossart, P., Griffiths, G. & Way, M. Actin-based motility of vaccinia
502 virus. *Nature* **378**, 636-638, doi:10.1038/378636a0 (1995).

503 11 Frischknecht, F. *et al*. Actin-based motility of vaccinia virus mimics receptor tyrosine
504 kinase signalling. *Nature* **401**, 926-929, doi:10.1038/44860 (1999).

505 12 Hollinshead, M. *et al*. Vaccinia virus utilizes microtubules for movement to the cell
506 surface. *J Cell Biol* **154**, 389-402, doi:10.1083/jcb.200104124 (2001).

bioRxiv preprint doi: https://doi.org/10.1101/2022.08.11.503617; this version posted October 17, 2022. The copyright holder for this preprint (which was not certified by peer review) is the author/funder, who has granted bioRxiv a license to display the preprint in perpetuity. It is made available under aCC-BY 4.0 International license.

13 Ward, B. M. & Moss, B. Vaccinia virus intracellular movement is associated with microtubules and independent of actin tails. *J Virol* **75**, 11651-11663, doi:10.1128/JVI.75.23.11651-11663.2001 (2001).

14 Weisberg, A. S. *et al*. Enigmatic origin of the poxvirus membrane from the endoplasmic reticulum shown by 3D imaging of vaccinia virus assembly mutants. *Proc Natl Acad Sci U S A* **114**, E11001-E11009, doi:10.1073/pnas.1716255114 (2017).

15 Moss, B. Poxvirus membrane biogenesis. *Virology* **479-480**, 619-626, doi:10.1016/j.virol.2015.02.003 (2015).

16 Chlanda, P., Carbajal, M. A., Cyrklaff, M., Griffiths, G. & Krijnse-Locker, J. Membrane rupture generates single open membrane sheets during vaccinia virus assembly. *Cell Host Microbe* **6**, 81-90, doi:10.1016/j.chom.2009.05.021 (2009).

17 Heuser, J. Deep-etch EM reveals that the early poxvirus envelope is a single membrane bilayer stabilized by a geodetic "honeycomb" surface coat. *J Cell Biol* **169**, 269-283, doi:10.1083/jcb.200412169 (2005).

18 Szajner, P., Weisberg, A. S., Lebowitz, J., Heuser, J. & Moss, B. External scaffold of spherical immature poxvirus particles is made of protein trimers, forming a honeycomb lattice. *J Cell Biol* **170**, 971-981, doi:10.1083/jcb.200504026 (2005).

19 Hyun, J., Matsunami, H., Kim, T. G. & Wolf, M. Assembly mechanism of the pleomorphic immature poxvirus scaffold. *Nat Commun* **13**, 1704, doi:10.1038/s41467-022-29305-5 (2022).

20 Bahar, M. W., Graham, S. C., Stuart, D. I. & Grimes, J. M. Insights into the evolution of a complex virus from the crystal structure of vaccinia virus D13. *Structure* **19**, 1011-1020, doi:10.1016/j.str.2011.03.023 (2011).

21 Garriga, D. *et al*. Structural basis for the inhibition of poxvirus assembly by the antibiotic rifampicin. *Proc Natl Acad Sci U S A* **115**, 8424-8429, doi:10.1073/pnas.1810398115 (2018).

22 Hyun, J. K. *et al*. Membrane remodeling by the double-barrel scaffolding protein of poxvirus. *PLoS Pathog* **7**, e1002239, doi:10.1371/journal.ppat.1002239 (2011).

23 Condit, R. C., Moussatche, N. & Traktman, P. In a nutshell: structure and assembly of the vaccinia virion. *Adv Virus Res* **66**, 31-124, doi:10.1016/S0065-3527(06)66002-8 (2006).

bioRxiv preprint doi: https://doi.org/10.1101/2022.08.11.503617; this version posted October 17, 2022. The copyright holder for this preprint (which was not certified by peer review) is the author/funder, who has granted bioRxiv a license to display the preprint in perpetuity. It is made available under aCC-BY 4.0 International license.

537 24 Ansarah-Sobrinho, C. & Moss, B. Role of the I7 protein in proteolytic processing of
538 vaccinia virus membrane and core components. *J Virol* **78**, 6335-6343,
539 doi:10.1128/JVI.78.12.6335-6343.2004 (2004).

540 25 Senkevich, T. G., White, C. L., Koonin, E. V. & Moss, B. Complete pathway for protein
541 disulfide bond formation encoded by poxviruses. *Proc Natl Acad Sci U S A* **99**, 6667-6672,
542 doi:10.1073/pnas.062163799 (2002).

543 26 Cyrklaff, M. *et al*. Cryo-electron tomography of vaccinia virus. *Proc Natl Acad Sci U*
544 *S A* **102**, 2772-2777, doi:10.1073/pnas.0409825102 (2005).

545 27 Dubochet, J., Adrian, M., Richter, K., Garces, J. & Wittek, R. Structure of
546 intracellular mature vaccinia virus observed by cryoelectron microscopy. *J Virol* **68**, 1935-
547 1941, doi:10.1128/JVI.68.3.1935-1941.1994 (1994).

548 28 Griffiths, G., Roos, N., Schleich, S. & Locker, J. K. Structure and assembly of
549 intracellular mature vaccinia virus: thin-section analyses. *J Virol* **75**, 11056-11070,
550 doi:10.1128/JVI.75.22.11056-11070.2001 (2001).

551 29 Mohandas, A. R. & Dales, S. Involvement of spicules in the formation of vaccinia virus
552 envelopes elucidated by a conditional lethal mutant. *Virology* **214**, 494-502,
553 doi:10.1006/viro.1995.0060 (1995).

554 30 Morgan, C. The insertion of DNA into vaccinia virus. *Science* **193**, 591-592,
555 doi:10.1126/science.959819 (1976).

556 31 Roos, N. *et al*. A novel immunogold cryoelectron microscopic approach to investigate
557 the structure of the intracellular and extracellular forms of vaccinia virus. *EMBO J* **15**, 2343-
558 2355 (1996).

559 32 Cyrklaff, M. *et al*. Whole cell cryo-electron tomography reveals distinct disassembly
560 intermediates of vaccinia virus. *PLoS One* **2**, e420, doi:10.1371/journal.pone.0000420
561 (2007).

562 33 Unger, B., Mercer, J., Boyle, K. A. & Traktman, P. Biogenesis of the vaccinia virus
563 membrane: genetic and ultrastructural analysis of the contributions of the A14 and A17
564 proteins. *J Virol* **87**, 1083-1097, doi:10.1128/JVI.02529-12 (2013).

bioRxiv preprint doi: https://doi.org/10.1101/2022.08.11.503617; this version posted October 17, 2022. The copyright holder for this preprint (which was not certified by peer review) is the author/funder, who has granted bioRxiv a license to display the preprint in perpetuity. It is made available under aCC-BY 4.0 International license.

565 34 Bisht, H., Weisberg, A. S., Szajner, P. & Moss, B. Assembly and disassembly of the
566 capsid-like external scaffold of immature virions during vaccinia virus morphogenesis. *J*
567 *Virol* **83**, 9140-9150, doi:10.1128/JVI.00875-09 (2009).

568 35 Faini, M., Beck, R., Wieland, F. T. & Briggs, J. A. Vesicle coats: structure, function,
569 and general principles of assembly. *Trends Cell Biol* **23**, 279-288,
570 doi:10.1016/j.tcb.2013.01.005 (2013).

571 36 Kirchhausen, T. Three ways to make a vesicle. *Nat Rev Mol Cell Biol* **1**, 187-198,
572 doi:10.1038/35043117 (2000).

573 37 Stachowiak, J. C., Brodsky, F. M. & Miller, E. A. A cost-benefit analysis of the physical
574 mechanisms of membrane curvature. *Nat Cell Biol* **15**, 1019-1027, doi:10.1038/ncb2832
575 (2013).

576 38 Stachowiak, J. C. *et al*. Membrane bending by protein-protein crowding. *Nat Cell*
577 *Biol* **14**, 944-949, doi:10.1038/ncb2561 (2012).

578 39 Erlandson, K. J. *et al*. Poxviruses Encode a Reticulon-Like Protein that Promotes
579 Membrane Curvature. *Cell Rep* **14**, 2084-2091, doi:10.1016/j.celrep.2016.01.075 (2016).

580 40 Sodeik, B. *et al*. Assembly of vaccinia virus: role of the intermediate compartment
581 between the endoplasmic reticulum and the Golgi stacks. *J Cell Biol* **121**, 521-541,
582 doi:10.1083/jcb.121.3.521 (1993).

583 41 Rodriguez, J. R., Risco, C., Carrascosa, J. L., Esteban, M. & Rodriguez, D. Vaccinia
584 virus 15-kilodalton (A14L) protein is essential for assembly and attachment of viral crescents
585 to virosomes. *J Virol* **72**, 1287-1296, doi:10.1128/JVI.72.2.1287-1296.1998 (1998).

586 42 Ericsson, M. *et al*. Characterization of ts 16, a temperature-sensitive mutant of
587 vaccinia virus. *J Virol* **69**, 7072-7086, doi:10.1128/JVI.69.11.7072-7086.1995 (1995).

588 43 Yeh, W. W., Moss, B. & Wolffe, E. J. The vaccinia virus A9L gene encodes a membrane
589 protein required for an early step in virion morphogenesis. *J Virol* **74**, 9701-9711,
590 doi:10.1128/jvi.74.20.9701-9711.2000 (2000).

591 44 Cudmore, S. *et al*. A vaccinia virus core protein, p39, is membrane associated. *J*
592 *Virol* **70**, 6909-6921, doi:10.1128/JVI.70.10.6909-6921.1996 (1996).

bioRxiv preprint doi: https://doi.org/10.1101/2022.08.11.503617; this version posted October 17, 2022. The copyright holder for this preprint (which was not certified by peer review) is the author/funder, who has granted bioRxiv a license to display the preprint in perpetuity. It is made available under aCC-BY 4.0 International license.

593 45 Wilton, S., Mohandas, A. R. & Dales, S. Organization of the vaccinia envelope and
594 relationship to the structure of intracellular mature virions. *Virology* **214**, 503-511,
595 doi:10.1006/viro.1995.0061 (1995).

596 46 Briggs, J. A. *et al*. The mechanism of HIV-1 core assembly: insights from three-
597 dimensional reconstructions of authentic virions. *Structure* **14**, 15-20,
598 doi:10.1016/j.str.2005.09.010 (2006).

599 47 Briggs, J. A., Wilk, T., Welker, R., Krausslich, H. G. & Fuller, S. D. Structural
600 organization of authentic, mature HIV-1 virions and cores. *EMBO J* **22**, 1707-1715,
601 doi:10.1093/emboj/cdg143 (2003).

602 48 Gray, R. D. M. *et al*. Nanoscale polarization of the entry fusion complex of vaccinia
603 virus drives efficient fusion. *Nat Microbiol* **4**, 1636-1644, doi:10.1038/s41564-019-0488-4
604 (2019).

605 49 Senkevich, T. G., Ward, B. M. & Moss, B. Vaccinia virus entry into cells is dependent
606 on a virion surface protein encoded by the A28L gene. *J Virol* **78**, 2357-2366,
607 doi:10.1128/jvi.78.5.2357-2366.2004 (2004).

608 50 Moss, B. Poxvirus cell entry: how many proteins does it take? *Viruses* **4**, 688-707,
609 doi:10.3390/v4050688 (2012).

610 51 Schmidt, F. I., Bleck, C. K., Helenius, A. & Mercer, J. Vaccinia extracellular virions
611 enter cells by macropinocytosis and acid-activated membrane rupture. *EMBO J* **30**, 3647-
612 3661, doi:10.1038/emboj.2011.245 (2011).

613 52 Mercer, J. & Helenius, A. Vaccinia virus uses macropinocytosis and apoptotic mimicry
614 to enter host cells. *Science* **320**, 531-535, doi:10.1126/science.1155164 (2008).

615 53 Janeczko, R. A., Rodriguez, J. F. & Esteban, M. Studies on the mechanism of entry
616 of vaccinia virus in animal cells. *Arch Virol* **92**, 135-150, doi:10.1007/BF01310068 (1987).

617 54 Carter, G. C., Law, M., Hollinshead, M. & Smith, G. L. Entry of the vaccinia virus
618 intracellular mature virion and its interactions with glycosaminoglycans. *J Gen Virol* **86**,
619 1279-1290, doi:10.1099/vir.0.80831-0 (2005).

620 55 Doms, R. W., Blumenthal, R. & Moss, B. Fusion of intra- and extracellular forms of
621 vaccinia virus with the cell membrane. *J Virol* **64**, 4884-4892, doi:10.1128/JVI.64.10.4884-
622 4892.1990 (1990).

bioRxiv preprint doi: https://doi.org/10.1101/2022.08.11.503617; this version posted October 17, 2022. The copyright holder for this preprint (which was not certified by peer review) is the author/funder, who has granted bioRxiv a license to display the preprint in perpetuity. It is made available under aCC-BY 4.0 International license.

623 56 Kilcher, S. *et al*. siRNA screen of early poxvirus genes identifies the AAA+ ATPase D5
624 as the virus genome-uncoating factor. *Cell Host Microbe* **15**, 103-112,
625 doi:10.1016/j.chom.2013.12.008 (2014).

626 57 Hutin, S. *et al*. Domain Organization of Vaccinia Virus Helicase-Primase D5. *J Virol*
627 **90**, 4604-4613, doi:10.1128/JVI.00044-16 (2016).

628 58 Moussatche, N. & Condit, R. C. Fine structure of the vaccinia virion determined by
629 controlled degradation and immunolocalization. *Virology* **475**, 204-218,
630 doi:10.1016/j.virol.2014.11.020 (2015).

631 59 Wang, N. *et al*. Architecture of African swine fever virus and implications for viral
632 assembly. *Science* **366**, 640-644, doi:10.1126/science.aaz1439 (2019).

633 60 Abrescia, N. G., Bamford, D. H., Grimes, J. M. & Stuart, D. I. Structure unifies the
634 viral universe. *Annu Rev Biochem* **81**, 795-822, doi:10.1146/annurev-biochem-060910-
635 095130 (2012).

636 61 Durkin, C. H. *et al*. RhoD Inhibits RhoC-ROCK-Dependent Cell Contraction via PAK6.
637 *Dev Cell* **41**, 315-329 e317, doi:10.1016/j.devcel.2017.04.010 (2017).

638 62 Lynn, H. *et al*. Loss of cytoskeletal transport during egress critically attenuates
639 ectromelia virus infection in vivo. *J Virol* **86**, 7427-7443, doi:10.1128/JVI.06636-11 (2012).

640 63 Snetkov, X., Weisswange, I., Pfanzelter, J., Humphries, A. C. & Way, M. NPF motifs
641 in the vaccinia virus protein A36 recruit intersectin-1 to promote Cdc42:N-WASP-mediated
642 viral release from infected cells. *Nat Microbiol* **1**, 16141, doi:10.1038/nmicrobiol.2016.141
643 (2016).

644 64 Cordeiro, J. V. *et al*. F11-mediated inhibition of RhoA signalling enhances the spread
645 of vaccinia virus in vitro and in vivo in an intranasal mouse model of infection. *PLoS One* **4**,
646 e8506, doi:10.1371/journal.pone.0008506 (2009).

647 65 Kremer, J. R., Mastronarde, D. N. & McIntosh, J. R. Computer visualization of three-
648 dimensional image data using IMOD. *J Struct Biol* **116**, 71-76, doi:10.1006/jsbi.1996.0013
649 (1996).

650 66 Xiong, Q., Morphew, M. K., Schwartz, C. L., Hoenger, A. H. & Mastronarde, D. N.
651 CTF determination and correction for low dose tomographic tilt series. *J Struct Biol* **168**,
652 378-387, doi:10.1016/j.jsb.2009.08.016 (2009).

bioRxiv preprint doi: https://doi.org/10.1101/2022.08.11.503617; this version posted October 17, 2022. The copyright holder for this preprint (which was not certified by peer review) is the author/funder, who has granted bioRxiv a license to display the preprint in perpetuity. It is made available under aCC-BY 4.0 International license.

67 Turonova, B., Schur, F. K. M., Wan, W. & Briggs, J. A. G. Efficient 3D-CTF correction for cryo-electron tomography using NovaCTF improves subtomogram averaging resolution to 3.4A. *J Struct Biol* **199**, 187-195, doi:10.1016/j.jsb.2017.07.007 (2017).

68 Liu, Y.-T. *et al*. Isotropic Reconstruction of Electron Tomograms with Deep Learning. *bioRxiv*, 2021.2007.2017.452128, doi:10.1101/2021.07.17.452128 (2021).

69 Castano-Diez, D., Kudryashev, M. & Stahlberg, H. Dynamo Catalogue: Geometrical tools and data management for particle picking in subtomogram averaging of cryo-electron tomograms. *J Struct Biol* **197**, 135-144, doi:10.1016/j.jsb.2016.06.005 (2017).

70 Bharat, T. A. M., Russo, C. J., Lowe, J., Passmore, L. A. & Scheres, S. H. W. Advances in Single-Particle Electron Cryomicroscopy Structure Determination applied to Sub-tomogram Averaging. *Structure* **23**, 1743-1753, doi:10.1016/j.str.2015.06.026 (2015).

71 Pettersen, E. F. *et al*. UCSF ChimeraX: Structure visualization for researchers, educators, and developers. *Protein Sci* **30**, 70-82, doi:10.1002/pro.3943 (2021).

72 Weisswange, I., Newsome, T. P., Schleich, S. & Way, M. The rate of N-WASP exchange limits the extent of ARP2/3-complex-dependent actin-based motility. *Nature* **458**, 87-91, doi:10.1038/nature07773 (2009).

bioRxiv preprint doi: https://doi.org/10.1101/2022.08.11.503617; this version posted October 17, 2022. The copyright holder for this preprint (which was not certified by peer review) is the author/funder, who has granted bioRxiv a license to display the preprint in perpetuity. It is made available under aCC-BY 4.0 International license.

670 **Legends**

671

672 **Figure 1. Cryo-ET of vaccinia infected cells.**

673 **A.** Schematic representation of vaccinia assembly and envelopment. D13-coated membrane
674 crescents close to form a spherical IV (membrane in red), which mature into brick shaped
675 IMV (membrane in blue) with a viral core that presents two concavities, occupied by the
676 flanked by two lateral bodies (black). IMV can be enveloped by a Golgi cisterna or endosomal
677 compartment (orange), resulting in the formation of triple membraned IEV, which can fuse
678 with the plasma membrane to liberate extracellular enveloped virions (EEV), which are
679 called CEV if they remain attached to the cell surface. **B.** Left: Central section of a
680 tomogram showing fully formed IV. The red arrow points at an IV with a lateral invagination.
681 Invaginations in other IV can be seen in the 3D-segmented model of the membrane of the
682 same tomogram (right) (See Movie 1). **C.** Tomogram middle view (left) and its corresponding
683 segmentation (right) of IMV (See Movie 2). A "cut corner" (magenta arrows) is apparent in
684 some IMV. Scalebars = 100 nm.

685

686 **Figure 2. The stages of imature virion (IV) assembly**

687 **A.** Tomogram section showing D13-coated membrane crescents with open ends (magenta
688 arrowheads). **B.** Tomogram sections of a crescent which is almost closed: the middle view
689 (left) reveals a membrane discontinuity (magenta arrowheads) while in a higher plane (+ 48
690 nm, right) the membrane is continuous (see Movie 3). **C.** Closed IV containing a condensed
691 nucleoid (outlined in magenta) with repeated structural features (magenta arrowheads). **D.**
692 Cytoplasmic condensed nucleoid/s next to an IV. **E.** Extended nucleoid/s associated with an
693 open IV. **F.** Structured illumination microscopy image of an infected cell showing condensed
694 DNA structures (green) in association with RFP-A3 positive viral particles (magenta) located
695 in a viral factory. Tomogram Scalebars = 100 nm.

696

697 **Figure 3. In situ structure of the D13 lattice.**

698 **A.** Tomogram section as indicated in the schematic on the left through the middle and top
699 of a representative IV (see Movie 4). The densities corresponding to the D13 lattice are
700 coloured in magenta in the right panels and show pseudo-hexagonal organisation. Scale bar
701 = 100 nm. **B.** Map based on subtomogram averaging of D13 and the underlying IV membrane
702 from a top (left) and a side (right) view with fitting of coordinate models of D13 trimers
703 (PDB 7VFE) shown in blue/brown.

704

705

bioRxiv preprint doi: https://doi.org/10.1101/2022.08.11.503617; this version posted October 17, 2022. The copyright holder for this preprint (which was not certified by peer review) is the author/funder, who has granted bioRxiv a license to display the preprint in perpetuity. It is made available under aCC-BY 4.0 International license.

Figure 4. Corrugation of the viral membrane during IV to IMV maturation.

A. Representative IV showing that the viral membrane is smooth. Magnified regions (2 x) are shown to the right, with or without a line tracing the IV membrane. The D13 lattice is marked with an asterisk and arrowheads indicate the viral membrane. **B.** A portion (680 x 65 nm) of the IV membrane was segmented and two segmentation views are shown illustrating its smoothness. **C.** Top left shows a middle section of an IMV, while the bottom left image corresponds to a "side view" of another IMV. In the magnified regions, a cyan line traces the wrinkled IMV membrane (Arrowheads). **D.** A portion (570-580 x 65 nm) of each viral membrane was segmented and two views are shown for each virion. Scale bars = 100 nm.

Figure 5. Ultrastructure of IMV.

A. Central tomogram section showing the broadest view of a representative IMV together with a region magnified 2.5-times to highlight the IMV layers (see Movie 5). **B.** Lateral view of an IMV, showing the lateral bodies (outlined in red) and the two concavities of the core. The magnified regions outlined in magenta show the IMV layers. **C.** Different sections of the IMV shown in A at the indicated plane positions in nm. The inset in the +31 nm view shows the surface of the palisade lattice. In the second row, yellow highlights the palisade structure, while red indicates the lateral body. **D.** The first row shows a schematic representation of the views displayed in C, while the second row represents the orthogonal view together with the tomogram position (black line). **E.** Left: Top and side views of a segmentation model of the IMV in A. The outer layer (blue) and viral membrane (black) are cut away so the internal palisade (yellow) and the lateral bodies (red) can be seen (see Movie 6). Right: The two concavities of the core are more apparent in a Simulated Digitally Reconstructed Radiograph (DDR Rendering) of the same segmentation model. Scale bars = 100 nm.

Figure 6. Ultrastructure of the naked viral core.

A. Middle section of a naked viral core together with a region magnified 3 times to highlight the palisade and inner wall as well as the polymers that surround the core. **B.** A higher tomogram section (+ 41 nm) of the same naked viral core highlighting the pseudohexagonal lattice of the palisade. **C.** At an even higher section (+58 nm), ring structures associated with the palisade are evident. The dimensions of the rings (n=25) from 5 naked cores are indicated together with the standard error of the mean. Scale bars = 100 nm.

bioRxiv preprint doi: https://doi.org/10.1101/2022.08.11.503617; this version posted October 17, 2022. The copyright holder for this preprint (which was not certified by peer review) is the author/funder, who has granted bioRxiv a license to display the preprint in perpetuity. It is made available under aCC-BY 4.0 International license.

Figure 7. The invariant architecture of the corrugated IMV membrane.

A. Central plane of tomograms showing that the additional membranes of IEV and CEV (associated with the plasma membrane, PM) do not alter the ultrastructure of the internal IMV. A Schematic representation illustrating the number of membranes of IMV, IEV and EEV/CEV is shown beneath the tomograms. **B.** Segmented membranes of the CEV shown in A, highlighting the corrugated character of the inner membrane, which is in contrast to the smooth outer membrane of the CEV. The images on the right show views of the segmented portions of the inner (cyan, 450 x 65 nm) and outer (orange, 520 x 65 nm) membranes. Scale bars = 100 nm.

Figure 8. The palisade is a pseudohexagonal lattice composed of trimeric proteins.

A. Sections through the palisade layer corresponding to the virions shown in Figure 7A. Scale bar = 10 nm. **B.** Map derived from subtomogram averaging showing the inner wall, palisade layer, viral membrane, and outer layer in surface representation (left) and corresponding sections of the map (right, greyscale).

Figure 9. Maturation of vaccinia virus: from IV to IMV.

A. Middle view dimensions of IV (diameter, n = 26; perimeter, n = 15) and IMV (major axis, n = 22; intermediate axis, n = 19; minor axis, n = 10; perimeter, n = 19) tomograms. * indicates that the IMV minor axis was calculated from the side views of 3 IMV and 7 IMV inside EEV (see methods). For volume calculation IV and IMV were assumed to be spheres and triaxial ellipsoids, respectively. **B.** Plots showing the individual values for perimeter and diameter / major axis (magenta lines in schematics below graph) of the IV, IMV and EEV/CEV. IV and IMV measurements were used to calculate the averages shown in A. The averages of the EEV inner-most membrane perimeter and major axis are 1074.46 nm ± 7.09 nm and 348.91 ± 1.87 nm, respectively. **C.** IV and IMV along with possible intermediates together with magnified regions (2.5-times) highlighting the different layers of each particle. Scale bar = 100 nm. **D.** Vaccinia maturation model: the palisade lattice (yellow) forms inside D13-coated IV, its maximum length being determined by the IV diameter. Following disassembly of the D13 lattice, the viral membrane acquires the shape of the palisade and becomes wrinkled. During this process, the presence of two lateral bodies (red) results in the deformation of the core, which adopts its characteristic biconcave shape.

bioRxiv preprint doi: https://doi.org/10.1101/2022.08.11.503617; this version posted October 17, 2022. The copyright holder for this preprint (which was not certified by peer review) is the author/funder, who has granted bioRxiv a license to display the preprint in perpetuity. It is made available under aCC-BY 4.0 International license.

Supplementary Table 1. Measurements and calculations of virion dimensions.

A. The middle-view perimeters, IV diameter, the major axis of IMV and EEV/CEV are shown, together with the standard error of the mean (SEM) and the number of viral particles measured. The intermediate and minor axes of IMV are also shown, as well as the IEV axes. Finally, the calculated volume of IV, IMV and IEV are provided. See Methods for details of dimension calculations. **B**. For the thickness of the inner wall and the outer layer, 5 different IMV were measured by tracing 5 different lines for each IMV, which correspond to the five measurements shown. To estimate the distance between the palisade and the viral membrane (with no lateral bodies) 5 IMV were used. For the distance between the palisade and the plasma membrane through lateral bodies 1 IMV and 4 EEV were included in the quantification. All values correspond to nm.

Supplementary Table 2. Cryo-ET data collection and STA processing.

Supplementary Figure 1. Low-magnification images of vaccinia infected HeLa cells on grids. A. The pink circle marks the position where the IV in Figure 1B were imaged. The image on the right is a magnification of the circled area and its surroundings. **B**. A cryo-EM image showing IV (magenta arrow) and IMV (green arrow) visualised at low magnification in cells over holes in the carbon support film. Scale bars = 10 (left) and 1 µm (right) (A) and 1 µm (B).

Supplementary Figure 2. Tomographic gallery of IV with nucleoids

Tomographic sections showing IV with an internal condensed nucleoid outlined in magenta in the bottom row. Scale bar = 100 nm.

Supplementary Figure 3. Examples of IMV with and without cut corners

A. Gallery of tomographic sections of IMV with no cut corner, with magnified regions (2x) to highlight the wrinkled viral membrane. **B.** IMV with cut or flattened corner/s (black arrowheads). The magnified region of the first IMV shows the corrugation of the viral membrane, as in A. Scale bars = 100 nm.

Supplementary Figure 4. Palisade maps from IMV, IEV and EEV/CEV.

A. Maps derived from subtomogram averaging IMV, IEV or EEV/CEV. A surface (top) and a cut-section view (bottom) are shown. **B**. Fourier Shell Correlation plots for palisade maps as well as for the D13 map. Curves are given for the corrected, unmasked, masked and masked with phase randomisations calculations.

bioRxiv preprint doi: https://doi.org/10.1101/2022.08.11.503617; this version posted October 17, 2022. The copyright holder for this preprint (which was not certified by peer review) is the author/funder, who has granted bioRxiv a license to display the preprint in perpetuity. It is made available under aCC-BY 4.0 International license.

Movie 1. IV overview.
Tomogram of an intracellular region accumulating IV, which corresponds to the section shown in Figure 1B. IV membranes are segmented in red

Movie 2. IMV overview.
Tomogram showing IMV in the cytoplasm, which corresponds to the section shown in Figure 1C. IMV membrane is segmented in blue, microtubules in red and the lumen of an ER-like compartment in yellow.

Movie 3. IV assembly. Tomogram of an IV with a pore on the viral membrane (pore labelled with magenta arrowheads). Sections of this tomograms are shown in Figure 2B.

Movie 4. Ultrastructure of IV.
Tomogram corresponding to the IV shown in Figure 3A. Scale bar = 100 nm.

Movie 5. Ultrastructure of IMV.
Tomogram of the IMV particle shown in Figure 5A. Scale bar = 100 nm.

Movie 6. Segmentation of an IMV. The movie shows the segmentation performed on the IMV from Figure 5A. Blue is the outer layer and black labels the viral membrane, while yellow corresponds to the palisade lattice and red to the lateral bodies.

Movie 7. Ultrastructure of the naked viral core.
Tomogram of the naked core shown in Figure 6. The central magenta square marks part of the palisade, the top magenta rectangle highlights the flexible polymer observed and the small magenta squares at the end of the movie outline the ring-like structures protruding from the palisade. Scale bar = 100 nm.

bioRxiv preprint doi: https://doi.org/10.1101/2022.08.11.503617; this version posted October 17, 2022. The copyright holder for this preprint (which was not certified by peer review) is the author/funder, who has granted bioRxiv a license to display the preprint in perpetuity. It is made available under aCC-BY 4.0 International license.

Supplementary Table 1. Measurements and calculations of virion dimensions.

A.

Middle view perimeter	Average (nm)	SEM	
IV	1106.39	8.58	n = 15
IMV	1087.75	11.25	n = 19
EEV / CEV	1074.46	7.09	n = 20

Diameter / major axis	Average (nm)	Standard Error of the Mean (SEM)	
IV	351.89	2.88	n = 26
IMV	351.70	3.31	n = 22
EEV / CEV	348.91	1.87	n = 22

IMV	Average (nm)	SEM	
Intermediate axis	280.53	3.66	n = 19
Minor axis*	198.04	4.94	n = 10 (3 IMV, 7 EEV)

IEV	Average (nm)	SEM	
Major axis	437.86	13.88	n = 7
Intermediate axis	383.45112	10.95	n = 7
Minor axis (estimation)	259.11		

	Calculated volume (nm^3)
IV	2.28×10^7
IMV	1.02×10^7
IEV	2.28×10^7

bioRxiv preprint doi: https://doi.org/10.1101/2022.08.11.503617; this version posted October 17, 2022. The copyright holder for this preprint (which was not certified by peer review) is the author/funder, who has granted bioRxiv a license to display the preprint in perpetuity. It is made available under aCC-BY 4.0 International license.

B.

Inner wall thickness (nm)	IMV1	IMV2	IMV3	IMV4	IMV5	Final average	Standard Deviation	SEM
1	4.89	4.12	2.08	4.43	3.72			
2	4.29	3.88	4.28	3.20	2.71			
3	3.54	4.21	4.75	3.11	4.78			
4	3.25	3.48	3.61	2.38	4.28			
5	3.91	4.02	2.81	6.05	4.20			
average	3.98	3.94	3.51	3.84	3.94	3.84	0.19	0.09

Outer layer thickness (nm)	IMV1	IMV2	IMV3	IMV4	IMV5	Final average	Standard Deviation	SEM
1	7.24	8.15	6.14	6.90	5.61			
2	7.51	7.14	7.25	6.52	7.31			
3	7.48	6.55	5.86	6.37	5.05			
4	6.40	7.12	6.03	6.96	6.63			
5	5.58	5.77	7.71	6.28	7.11			
average	6.84	6.95	6.60	6.61	6.34	6.67	0.11	0.24

Palisade-to-viral membrane distance (nm)	IMV1	IMV3	IMV4	IMV5	Final average	Standard Deviation	SEM
1	9.54	10.12	8.89	9.47			
2	9.57	9.37	7.87	8.08			
3	11.18	9.51	8.32	8.31			
4	8.89	9.57	11.28	10.98			
5	8.66	8.53	7.36	10.04			
average	9.57	9.42	8.74	9.38	9.28	0.18	0.36

Palisade to viral membrane through lateral bodies (nm)	IMV1	EEV1	EEV2	EEV3	EEV4	Average	Standard Deviation	SEM
1	53.20	50.35	43.45	52.01	41.76			
2	31.93	48.19	42.39	62.64	39.35	46.53	8.60	2.72

bioRxiv preprint doi: https://doi.org/10.1101/2022.08.11.503617; this version posted October 17, 2022. The copyright holder for this preprint (which was not certified by peer review) is the author/funder, who has granted bioRxiv a license to display the preprint in perpetuity. It is made available under aCC-BY 4.0 International license.

Supplementary Table S2. Cryo-ET data collection and STA processing.

	Palisade				D13
	Combined	EEV/CEV	IMV	IEV	
Data collection					
Voltage (kV)	300				
Cumulative electron dose (e / Å^2)	66.3				
Applied defocus (μm)	-8				
Pixel size (Å)	4.31				
Tilt range (°)	±57°, dose symmetric				
STA processing					
Map symmetry	C3	C3	C3	C3	C6
Initial particle number	182938	209703	80698	8256	341376
Final particle number	179822	149662	27590	5686	34092
Map resolution (Å) (FSC=0.143)	21.2	21.2	25.1	30.6	19.2

bioRxiv preprint doi: https://doi.org/10.1101/2022.08.11.503617; this version posted October 17, 2022. The copyright holder for this preprint (which was not certified by peer review) is the author/funder, who has granted bioRxiv a license to display the preprint in perpetuity. It is made available under aCC-BY 4.0 International license.

A

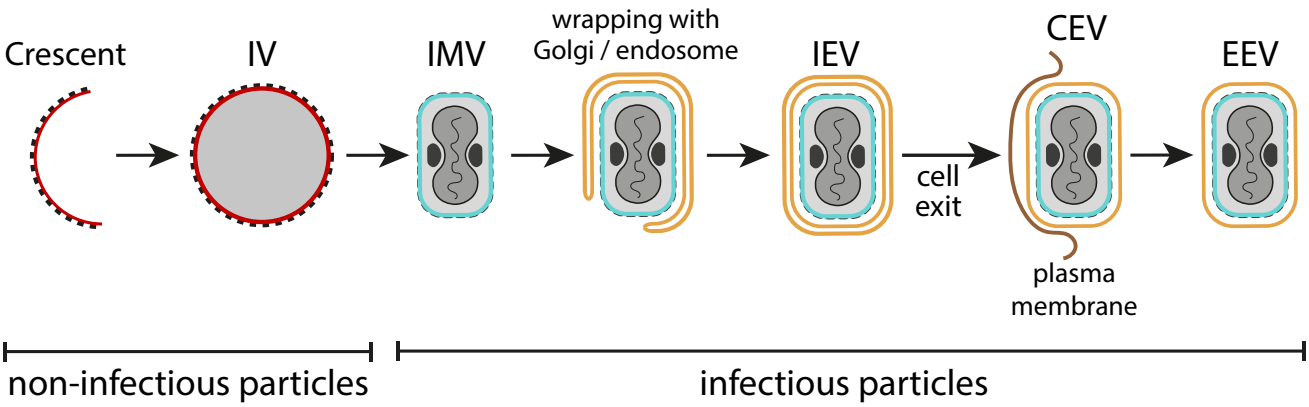

B

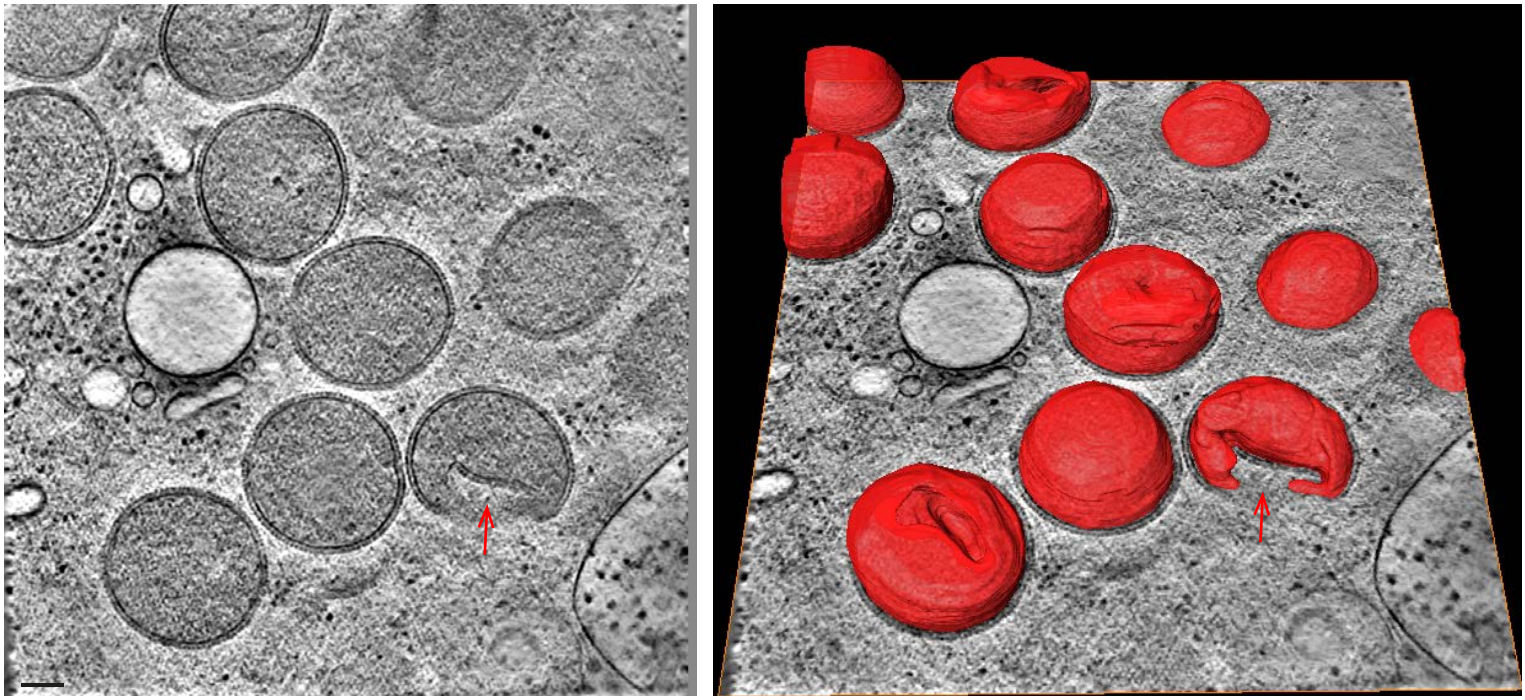

C

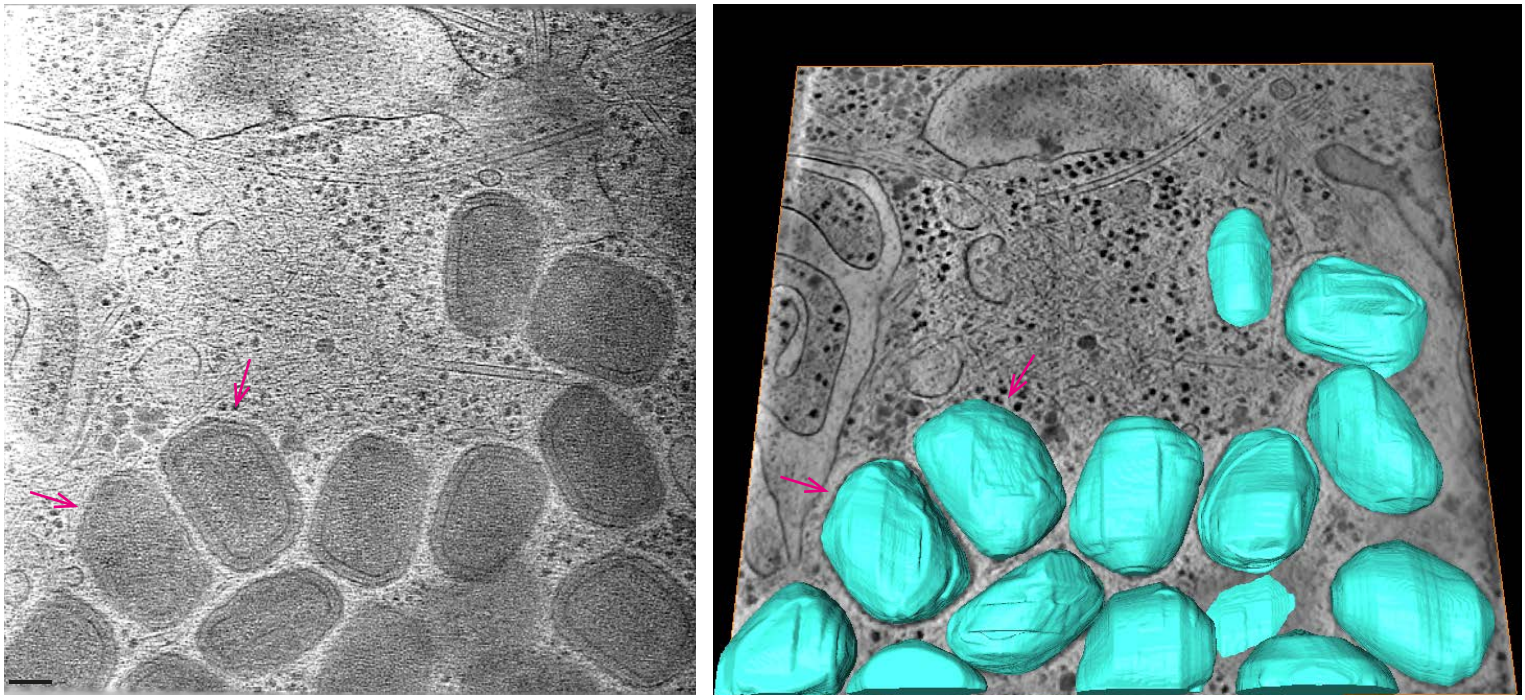

Figure 1

bioRxiv preprint doi: https://doi.org/10.1101/2022.08.11.503617; this version posted October 17, 2022. The copyright holder for this preprint (which was not certified by peer review) is the author/funder, who has granted bioRxiv a license to display the preprint in perpetuity. It is made available under aCC-BY 4.0 International license.

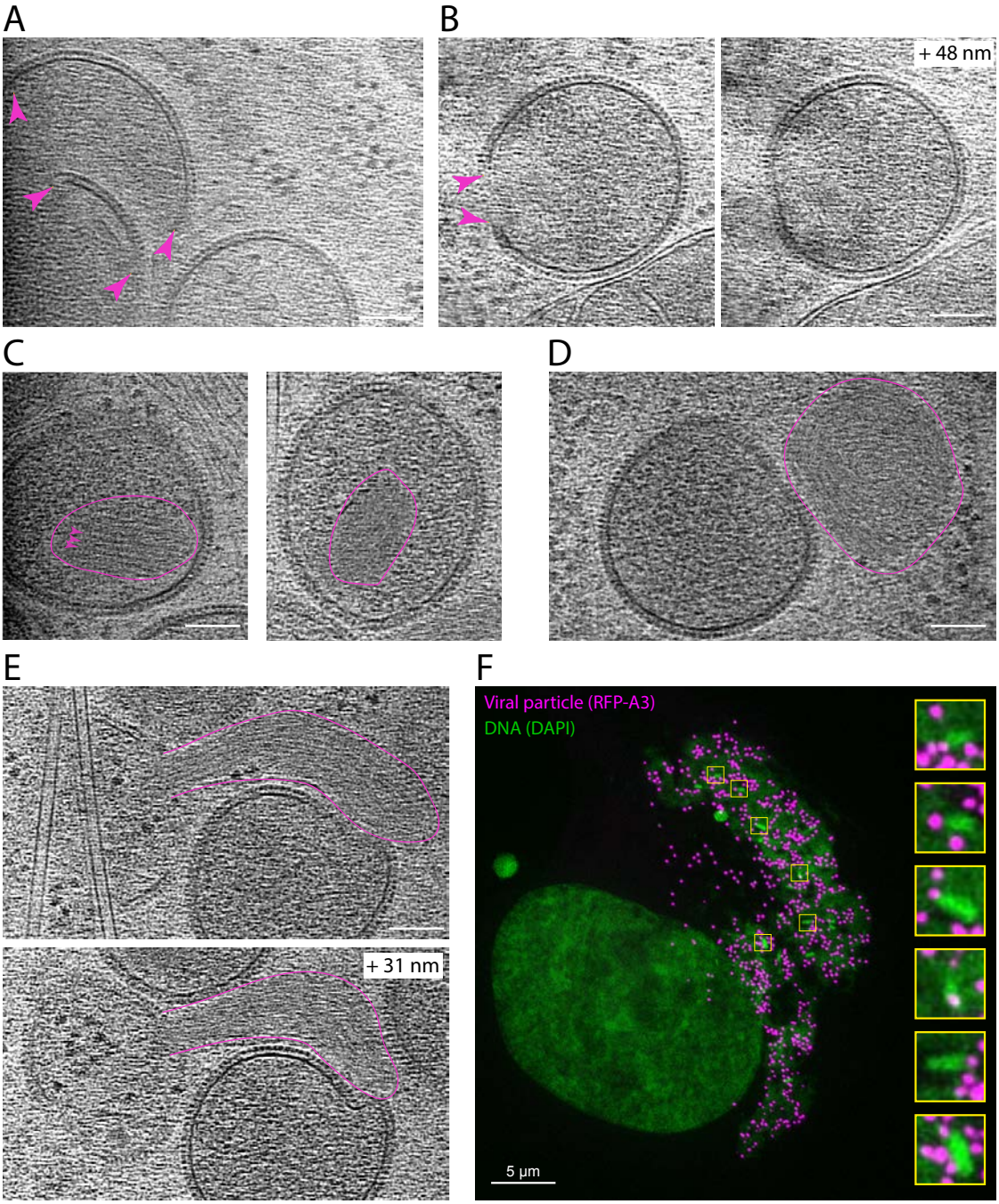

Figure 2

bioRxiv preprint doi: https://doi.org/10.1101/2022.08.11.503617; this version posted October 17, 2022. The copyright holder for this preprint (which was not certified by peer review) is the author/funder, who has granted bioRxiv a license to display the preprint in perpetuity. It is made available under aCC-BY 4.0 International license.

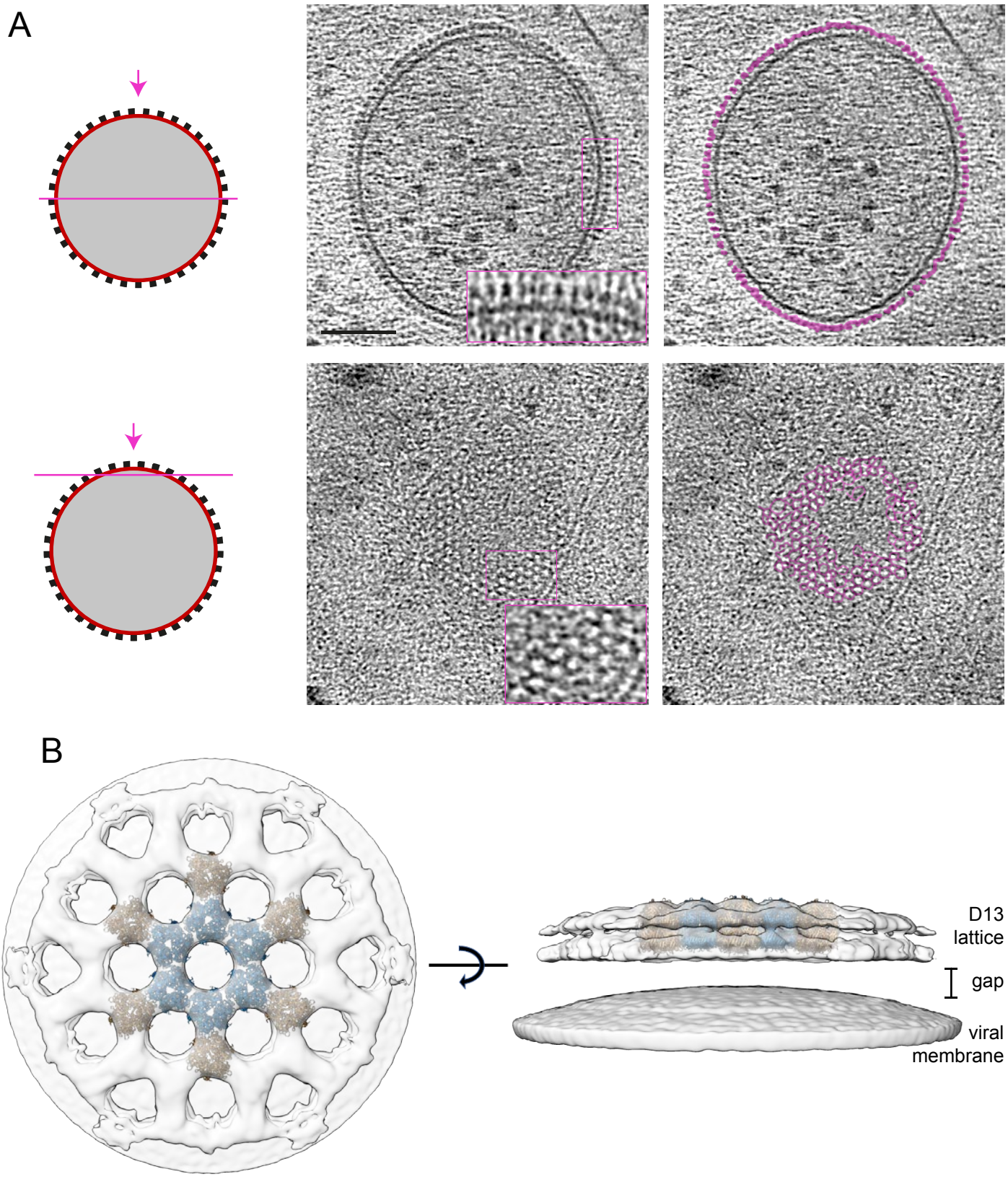

Figure 3

bioRxiv preprint doi: https://doi.org/10.1101/2022.08.11.503617; this version posted October 17, 2022. The copyright holder for this preprint (which was not certified by peer review) is the author/funder, who has granted bioRxiv a license to display the preprint in perpetuity. It is made available under aCC-BY 4.0 International license.

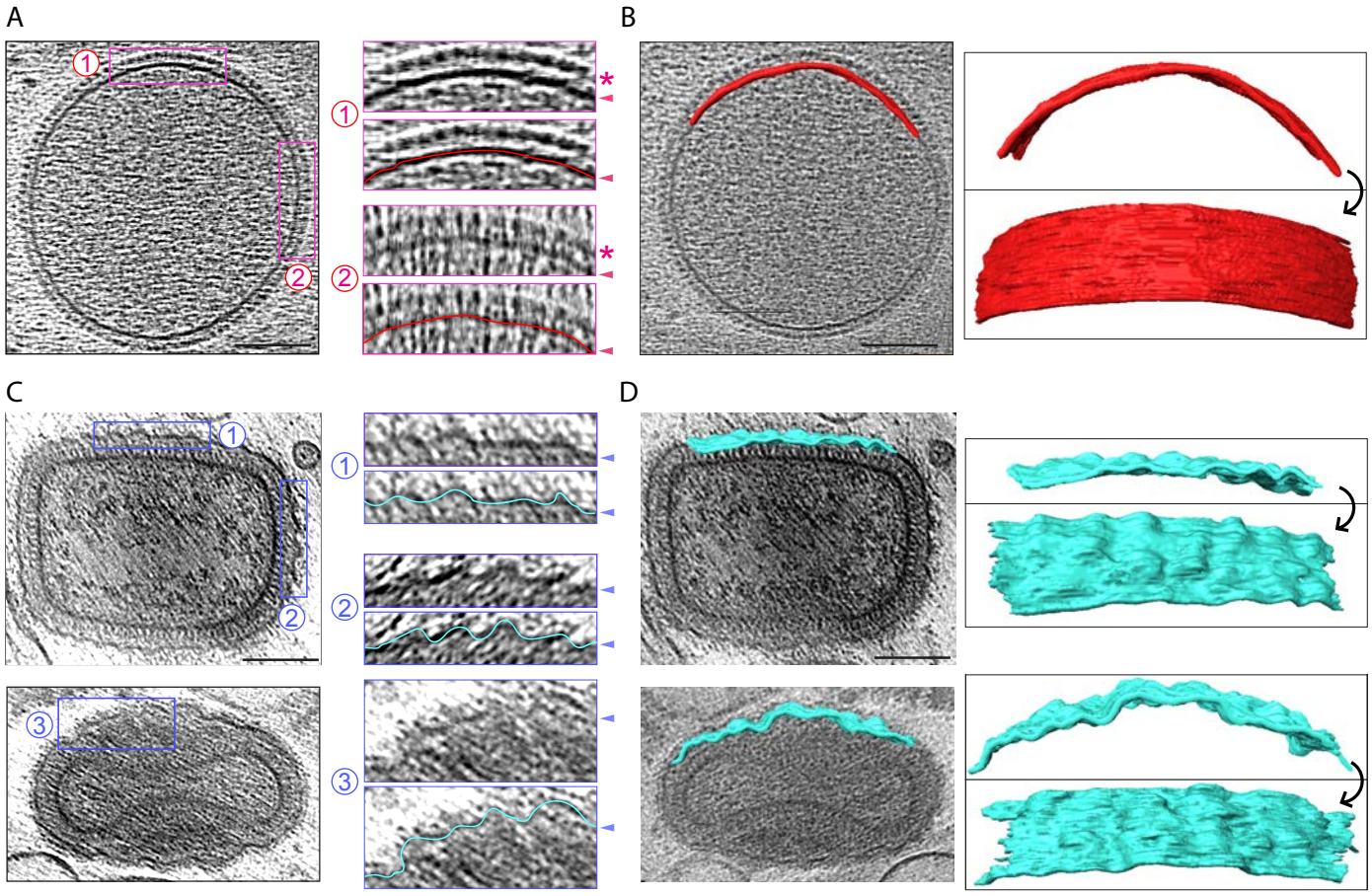

Figure 4

bioRxiv preprint doi: https://doi.org/10.1101/2022.08.11.503617; this version posted October 17, 2022. The copyright holder for this preprint (which was not certified by peer review) is the author/funder, who has granted bioRxiv a license to display the preprint in perpetuity. It is made available under aCC-BY 4.0 International license.

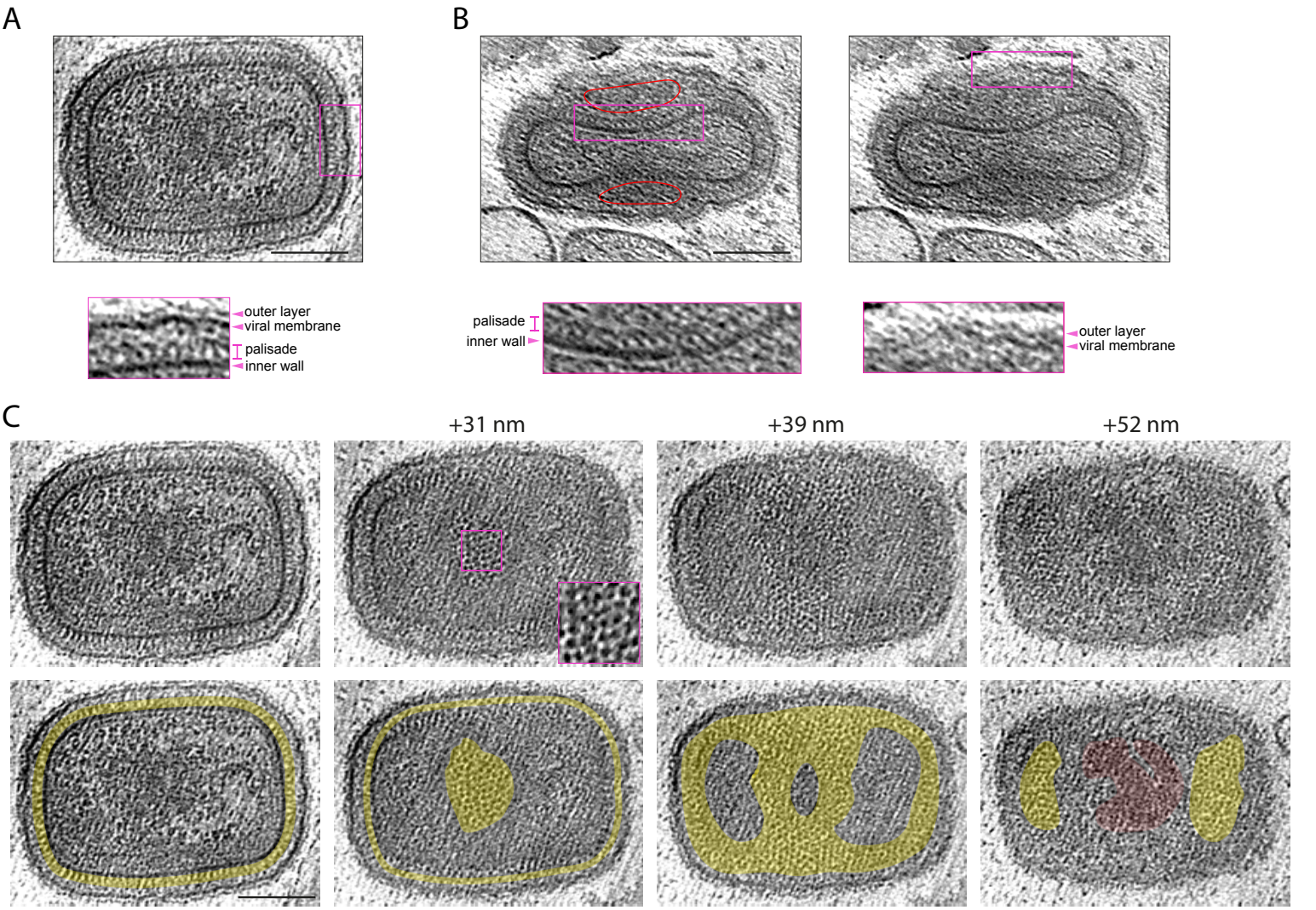

Figure 5

bioRxiv preprint doi: https://doi.org/10.1101/2022.08.11.503617; this version posted October 17, 2022. The copyright holder for this preprint (which was not certified by peer review) is the author/funder, who has granted bioRxiv a license to display the preprint in perpetuity. It is made available under aCC-BY 4.0 International license.

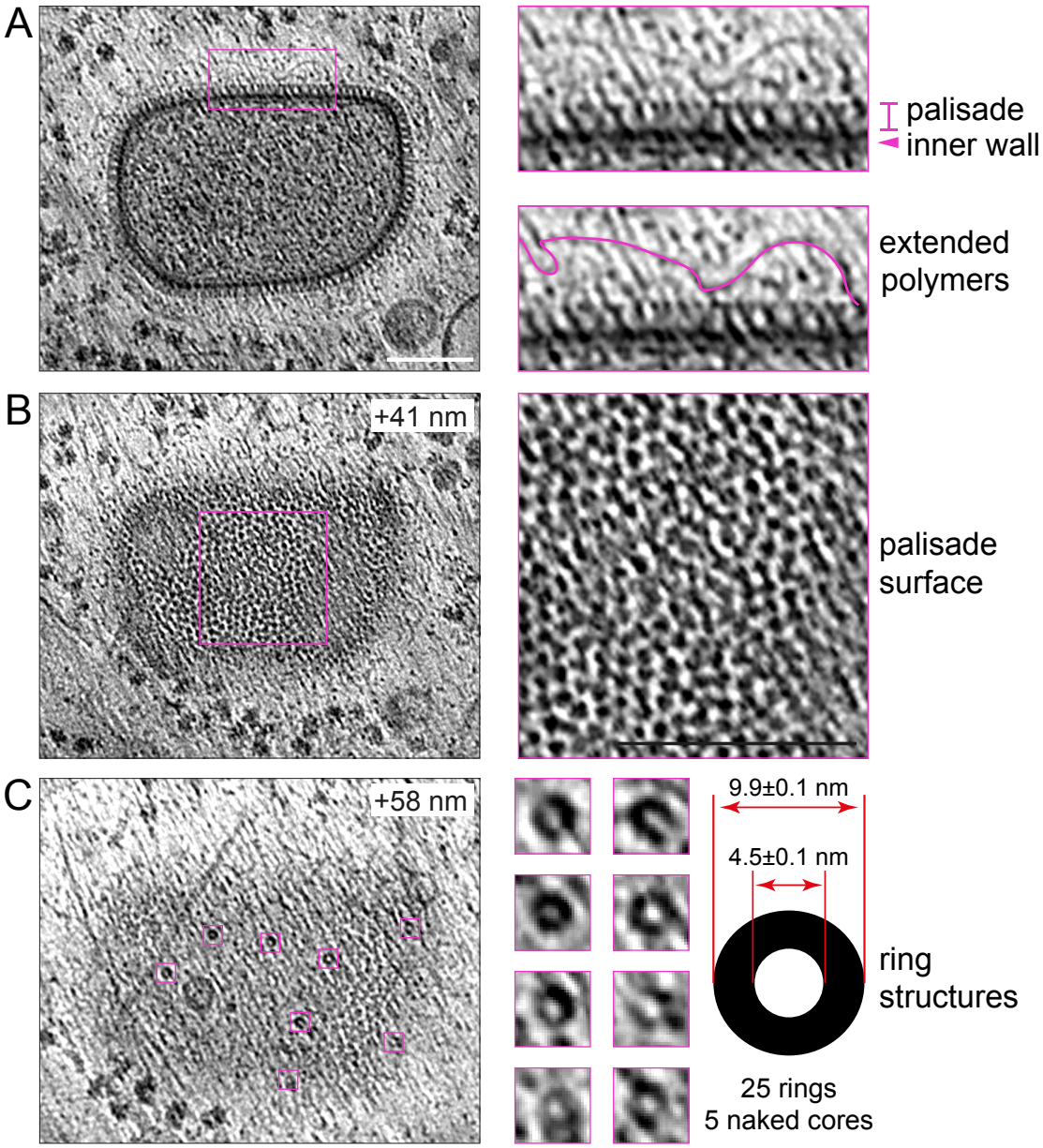

Figure 6

bioRxiv preprint doi: https://doi.org/10.1101/2022.08.11.503617; this version posted October 17, 2022. The copyright holder for this preprint (which was not certified by peer review) is the author/funder, who has granted bioRxiv a license to display the preprint in perpetuity. It is made available under aCC-BY 4.0 International license.

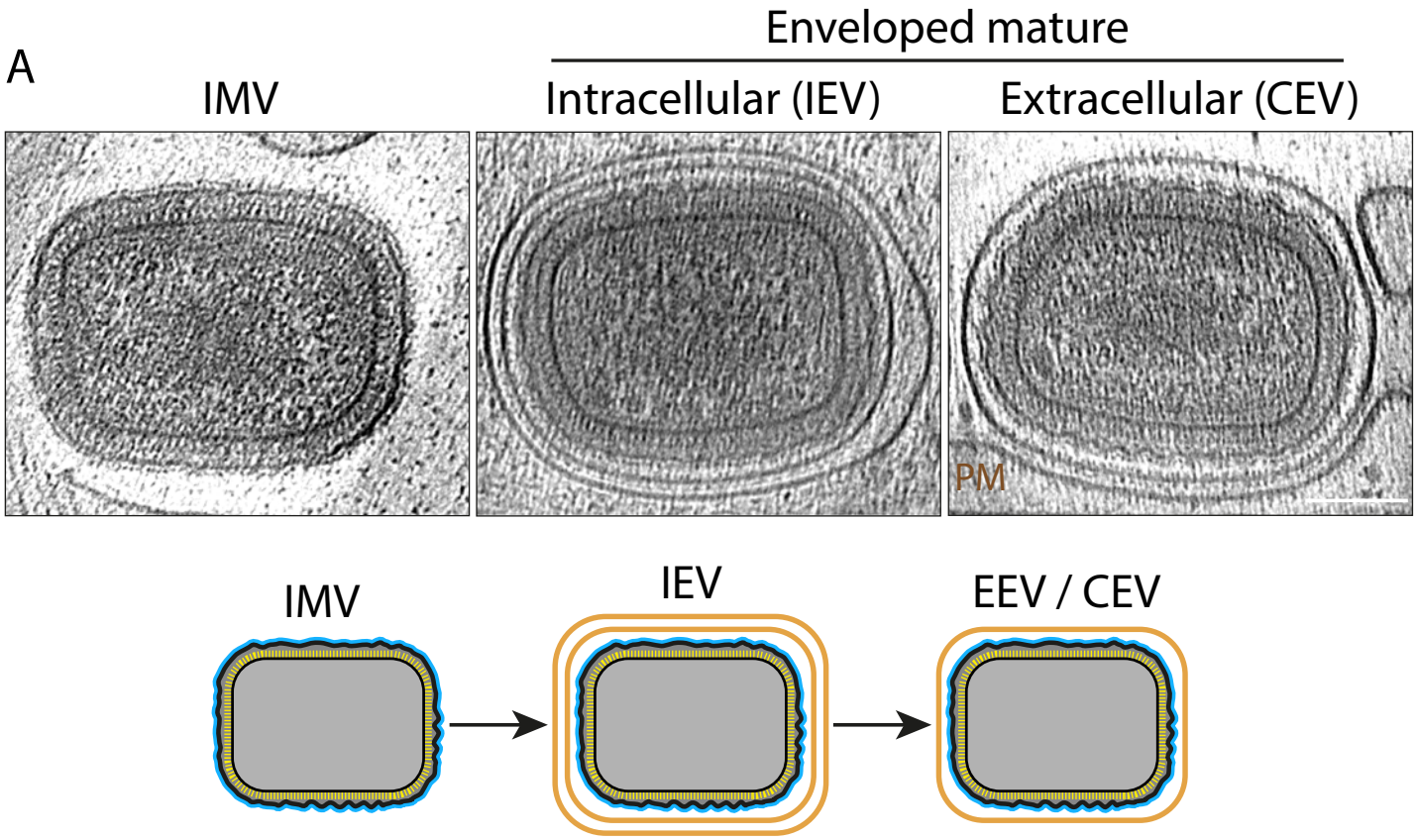

Figure 7

bioRxiv preprint doi: https://doi.org/10.1101/2022.08.11.503617; this version posted October 17, 2022. The copyright holder for this preprint (which was not certified by peer review) is the author/funder, who has granted bioRxiv a license to display the preprint in perpetuity. It is made available under aCC-BY 4.0 International license.

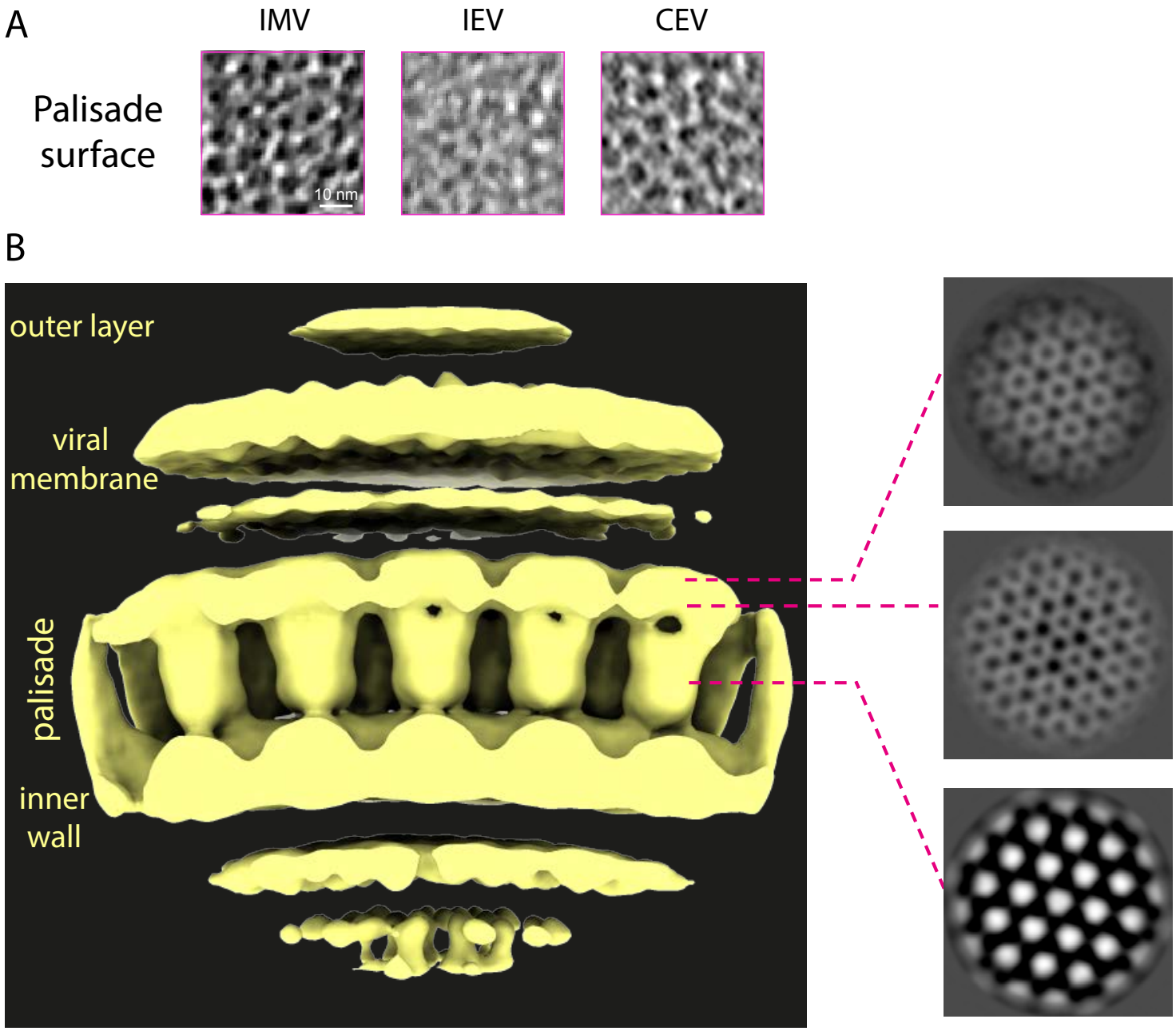

Figure 8

bioRxiv preprint doi: https://doi.org/10.1101/2022.08.11.503617; this version posted October 17, 2022. The copyright holder for this preprint (which was not certified by peer review) is the author/funder, who has granted bioRxiv a license to display the preprint in perpetuity. It is made available under aCC-BY 4.0 International license.

A

	Immature virus (IV)		Intracellular mature virus (IMV)	
Approximate shape	Sphere		Triaxial ellipsoid	
Dimensions (nm)	Diameter	351.89 ± 2.88	Major axis	351.70 ± 3.31
			Intermediate axis	280.53 ± 3.66
			Minor axis*	198.04 ± 4.94
Perimeter (middle plane, (nm)	1106.39 ± 8.58		1087.75 ± 11.25	
Calculated volume (nm^3)	2.28×10^7		1.02×10^7	

B

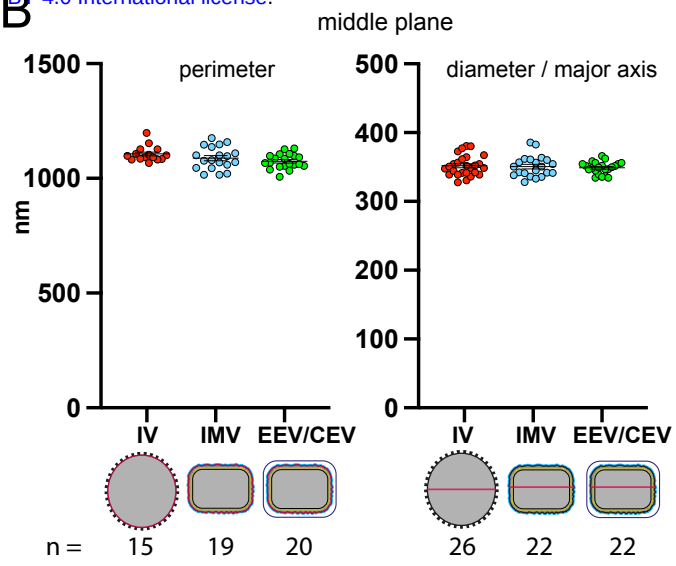

C

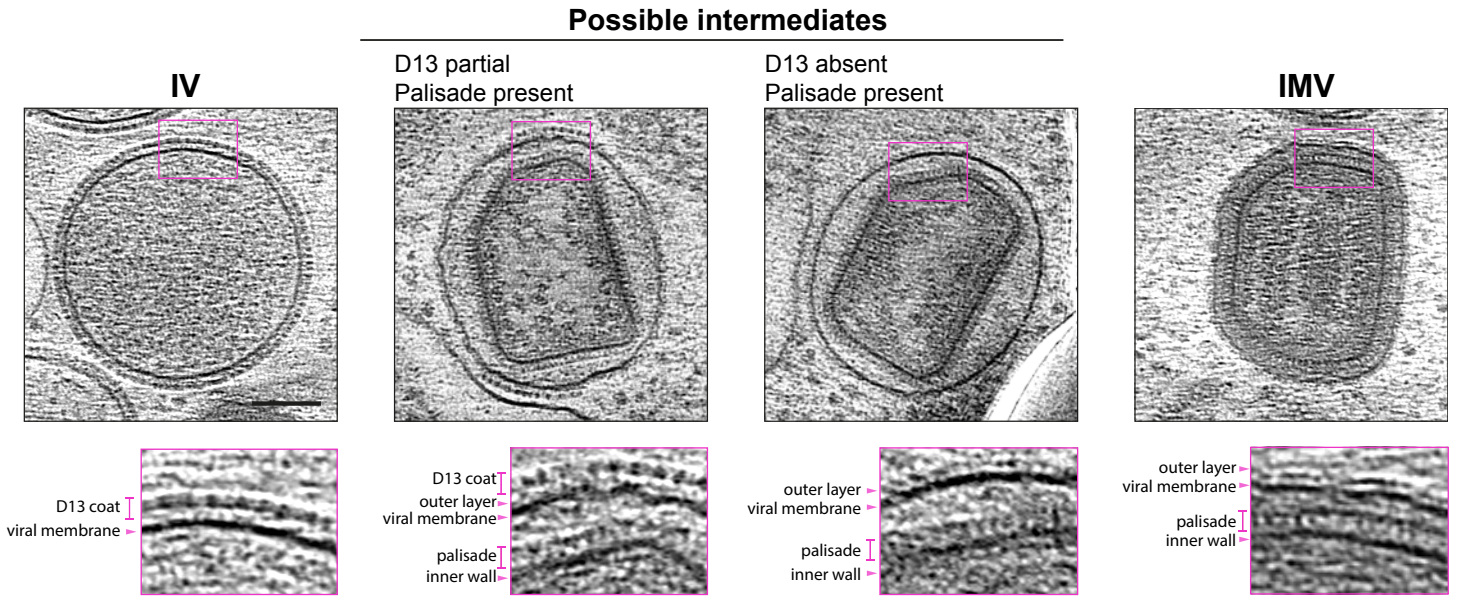

D

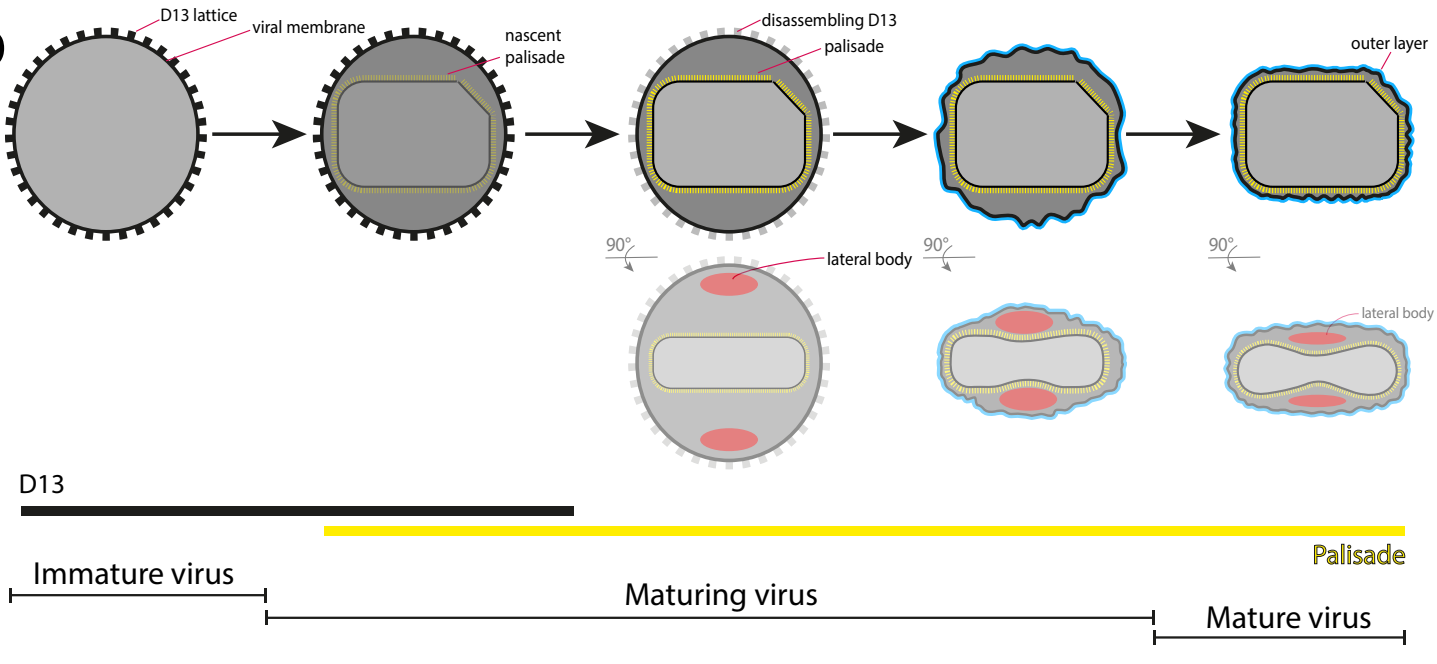

Figure 9

bioRxiv preprint doi: https://doi.org/10.1101/2022.08.11.503617; this version posted October 17, 2022. The copyright holder for this preprint (which was not certified by peer review) is the author/funder, who has granted bioRxiv a license to display the preprint in perpetuity. It is made available under aCC-BY 4.0 International license.

A

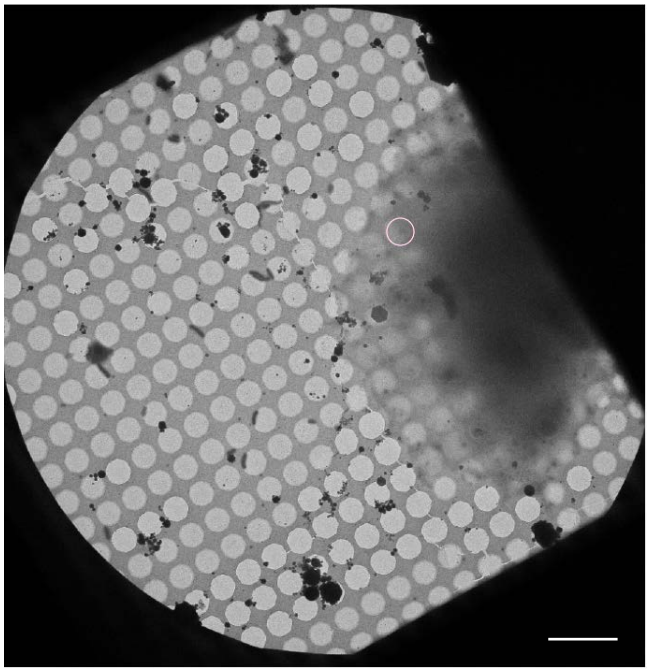

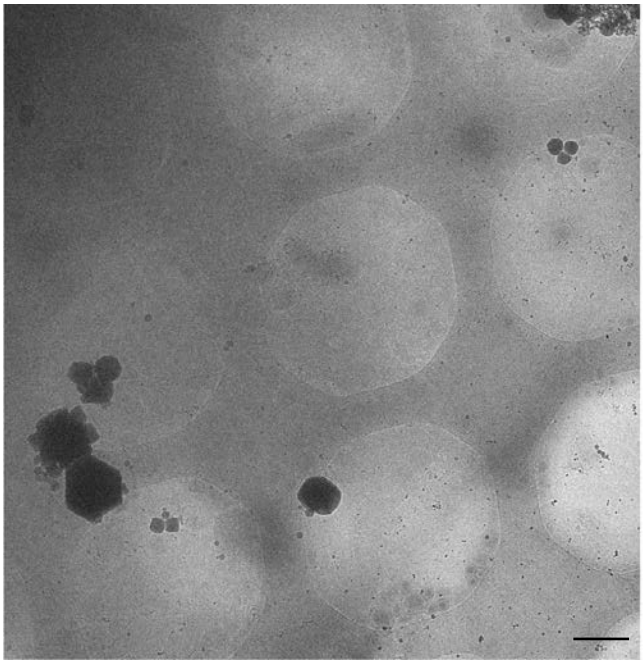

B

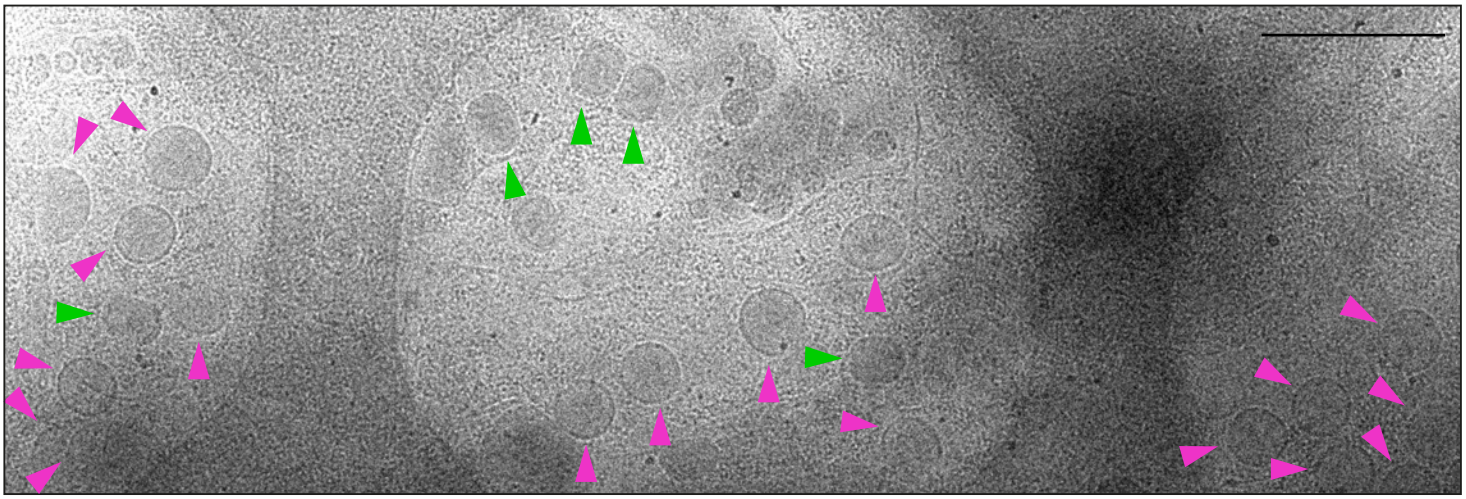

Supplementary Figure 1

bioRxiv preprint doi: https://doi.org/10.1101/2022.08.11.503617; this version posted October 17, 2022. The copyright holder for this preprint (which was not certified by peer review) is the author/funder, who has granted bioRxiv a license to display the preprint in perpetuity. It is made available under aCC-BY 4.0 International license.

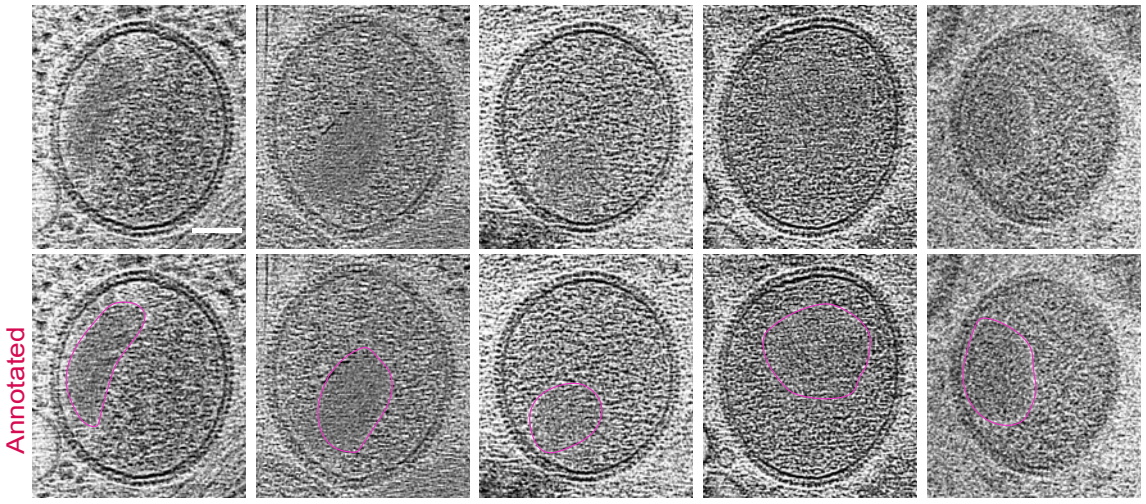

Supplementary Figure 2

bioRxiv preprint doi: https://doi.org/10.1101/2022.08.11.503617; this version posted October 17, 2022. The copyright holder for this preprint (which was not certified by peer review) is the author/funder, who has granted bioRxiv a license to display the preprint in perpetuity. It is made available under aCC-BY 4.0 International license.

A

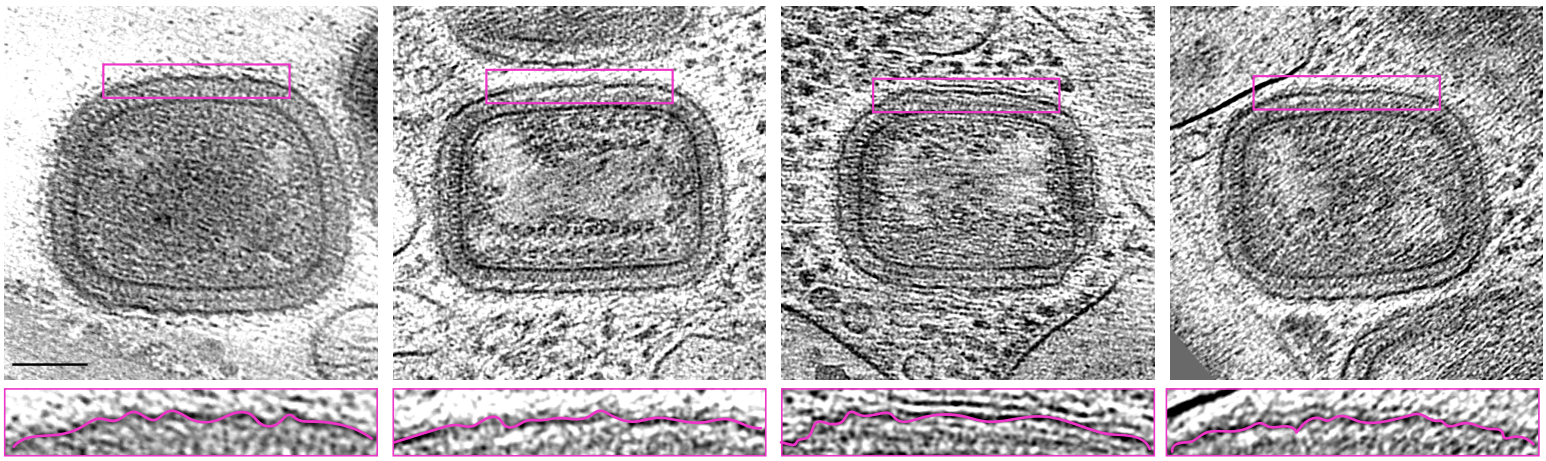

B

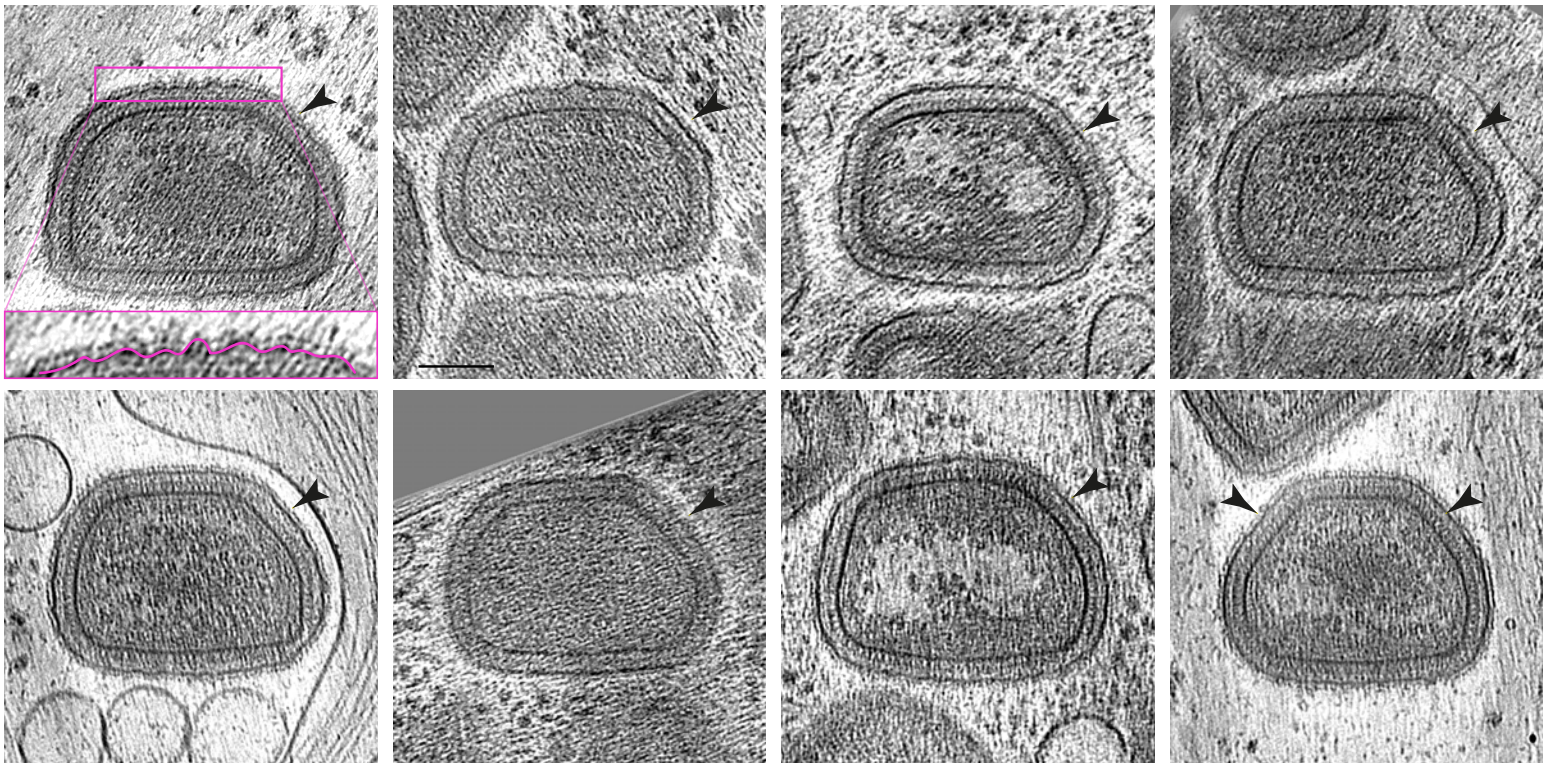

Cut corner : 48.9% No cut corner : 51.1% n = 94 IMV

Supplementary Figure 3

bioRxiv preprint doi: https://doi.org/10.1101/2022.08.11.503617; this version posted October 17, 2022. The copyright holder for this preprint (which was not certified by peer review) is the author/funder, who has granted bioRxiv a license to display the preprint in perpetuity. It is made available under aCC-BY 4.0 International license.

A

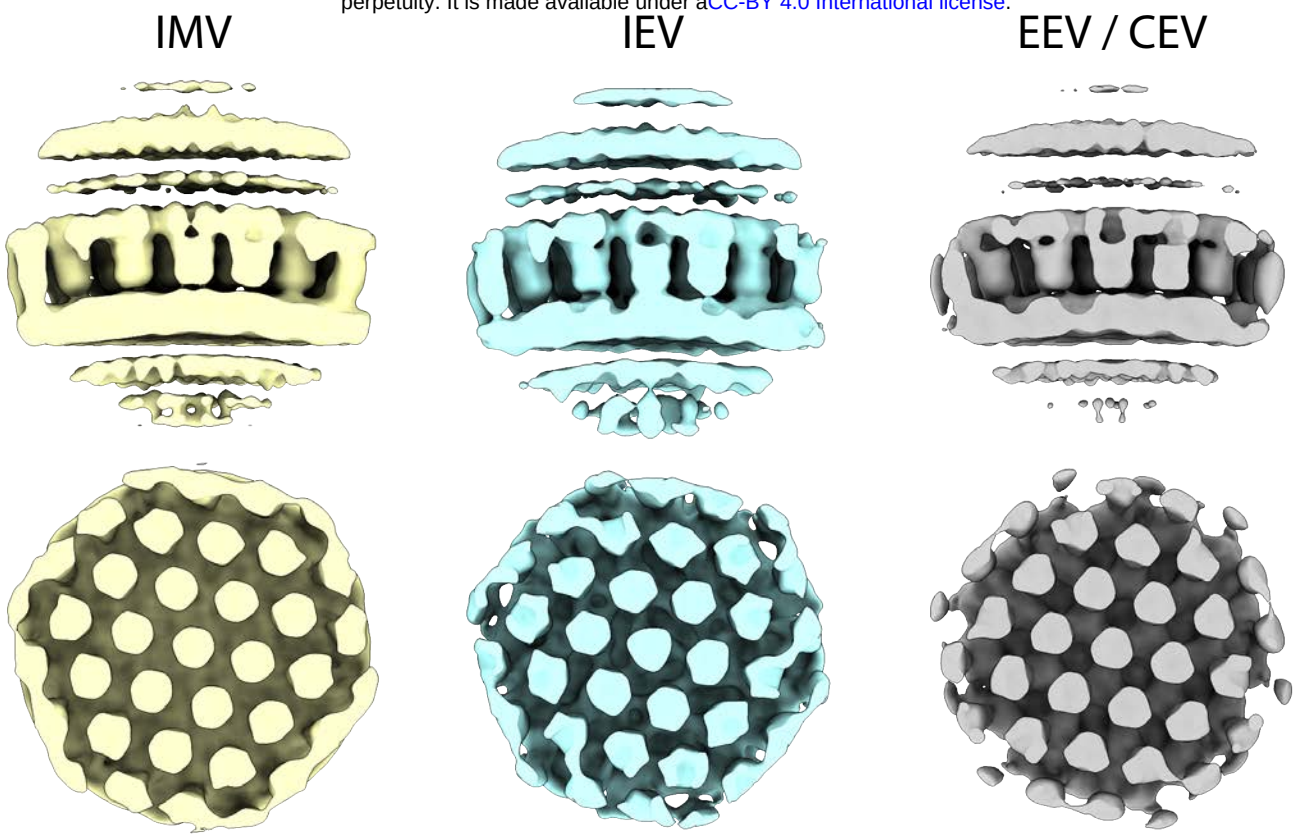

B

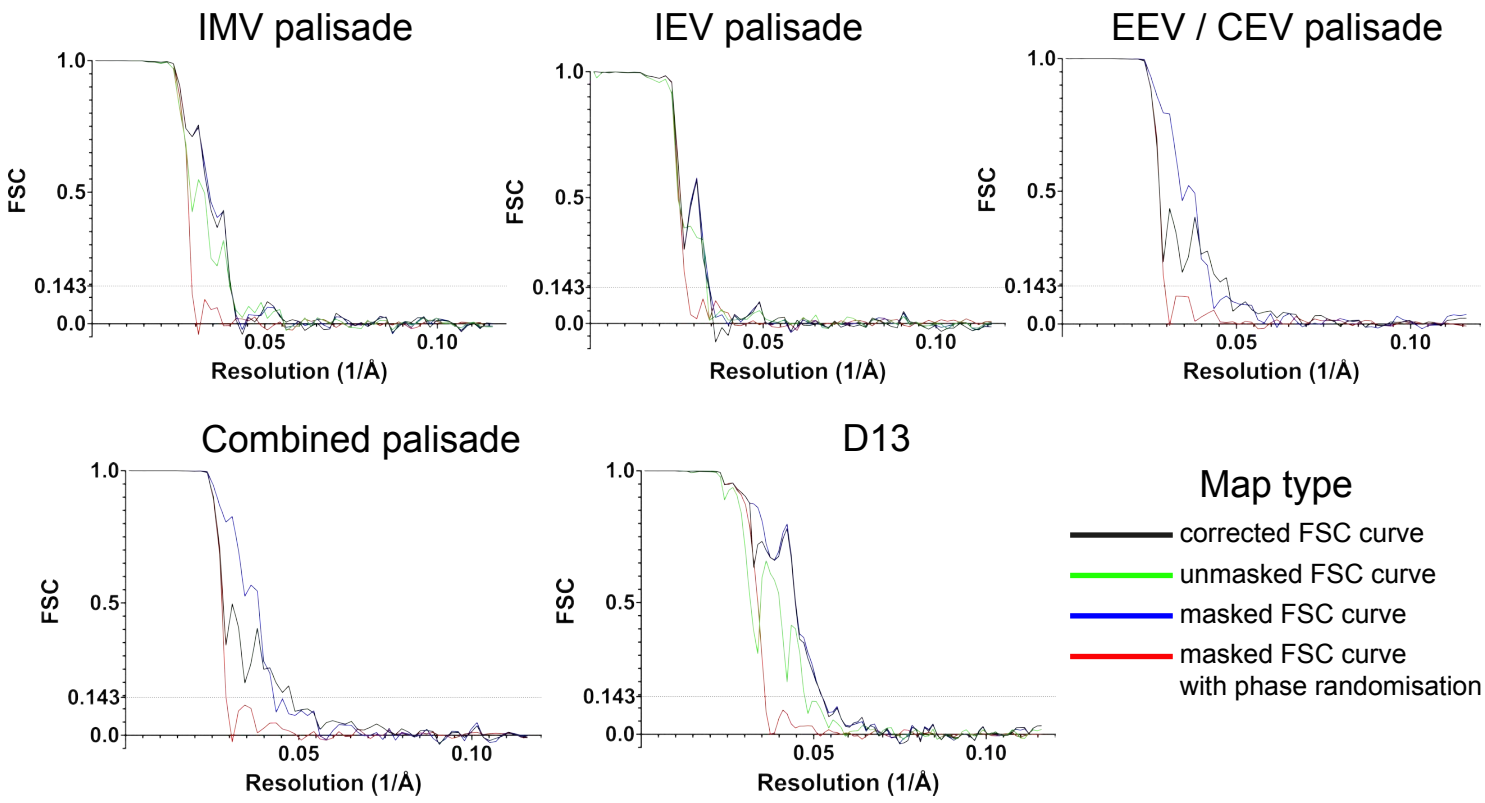

Supplementary Figure 4